Journal of Structural Geology 32 (2010) 855–875

Contents lists available at ScienceDirect

Journal of Structural Geology

journal homepage: www.elsevier.com/locate/jsg

Review Article

Interpretation and analysis of planetary structures

Richard A. Schultz [a,*], Ernst Hauber [b], Simon A. Kattenhorn [c], Chris H. Okubo [d], Thomas R. Watters [e]

[a] Geomechanics-Rock Fracture Group, Department of Geological Sciences and Engineering/172, University of Nevada, Reno, NV 89557-0138, United States
[b] DLR-Institut für Planetenforschung, Rutherfordstrasse 2, D-12489 Berlin-Adlershof, Germany
[c] Department of Geological Sciences, University of Idaho, P.O. Box 443022, Moscow, ID 83844-3022, United States
[d] U.S. Geological Survey, 2255 North Gemini Drive, Flagstaff, AZ 86001, United States
[e] Center for Earth and Planetary Studies, National Air and Space Museum, Smithsonian Institution, Washington, DC 20560, United States

ARTICLE INFO

Article history:
Received 24 April 2009
Received in revised form
31 August 2009
Accepted 13 September 2009
Available online 11 December 2009

Keywords:
Planetary structural geology
Faulting
Folding
Deformation bands
Joints
Fracture mechanics

ABSTRACT

Structural geology is an integral part of planetary science. Planetary structures provide the framework for determining the character and sequence of crustal deformation while simultaneously establishing the observational basis required to test geodynamic hypotheses for the deformation of planetary and satellite lithospheres. The availability of datasets that record spatial and topographic information with a resolution that matches or, in many cases, exceeds, what is available for Earth-based studies permits the deformation of several planets and satellites to be investigated down to the local or outcrop scales. The geometry and kinematics of common planetary structures such as joints, igneous dikes, deformation bands, faults, and folds can be determined with confidence from their distinctive morphologic and topographic signatures, enabling the structural histories and deformation magnitudes to be determined. Segmentation, displacement profiles, relay ramps, footwall anticlines, displacement-controlled depocenters, and other well-known characteristics of terrestrial normal fault and graben systems reveal the sequence and processes of fault growth in numerous planetary examples. Systems of thrust faults having both blind and surface-breaking components are important elements on several bodies including Mercury, the Moon, and Mars. Strike-slip faults have been identified on bodies including Mars and Europa with oblique extension found on Ganymede. Using field-based studies of Earth-based structures as a guide, planetary structures provide a means to explore and evaluate the causative stresses. Despite the wide range in structural styles across the solar system, plate tectonics is recognized only on the Earth, with the other planets and satellites deforming in the absence of large-scale horizontal motions and attendant plate recycling.

© 2010 Elsevier Ltd. All rights reserved.

1. Introduction

Deformation of the lithospheres of planets and satellites has produced populations of structures that appear to be strikingly similar to those found on Earth (see Watters and Schultz, 2010, for a comprehensive overview), both morphologically and mechanically. Faults in particular have been documented on nearly every geologic surface in the solar system, occurring in both lower-strain distributed and higher-strain localized regimes. Normal faults and grabens are found on Mercury, Venus, the Moon, Mars, and icy satellites of the outer planets such as Europa, Ganymede, Miranda, Ariel, Dione, Tethys, Rhea, and Titania (e.g., Watters and Schultz, 2010). Thrust faults have been recognized on Mercury, Venus, the Moon, Mars, and Io along with their surficial anticlines, called wrinkle ridges (Plescia and Golombek, 1986; Watters, 1988; Schenk and Bulmer, 1998; Schultz, 2000a; Okubo and Schultz, 2004). Arcuate fold belts related to contractional strain have been identified in the icy lithospheric shell of Enceladus (Porco et al., 2006), and rare folding has also been inferred on Europa (Prockter and Pappalardo, 2000). Strike-slip faults have been identified on Mars (e.g., Schultz, 1989; Okubo and Schultz, 2006a; Andrews-Hanna et al., 2008) and the icy satellites Europa (Schenk and McKinnon, 1989; Hoppa et al., 1999a; Kattenhorn, 2004; Kattenhorn and Marshall, 2006) and Ganymede (in association with normal faulting; DeRemer and Pappalardo, 2003; Pappalardo and Collins, 2005). Individual dilatant cracks (joints; Schultz and Fossen, 2008) have been identified on Mars (Okubo and McEwen, 2007; Okubo et al., 2009) and are pervasive on icy moons of the outer solar system such as Europa (Figueredo and Greeley, 2000, 2004; Kattenhorn, 2002; Marshall and Kattenhorn, 2005) and Enceladus (Kargel and Pozio, 1996; Porco et al., 2006). Deformation bands (Aydin et al., 2006; Fossen et al., 2007) have been identified on Mars (Okubo and McEwen, 2007; Okubo et al., 2009) and have been suggested to occur on Europa (Aydin, 2006). The presence of subsurface igneous

* Corresponding author.
E-mail address: schultz@mines.unr.edu (R.A. Schultz).

0191-8141/$ – see front matter © 2010 Elsevier Ltd. All rights reserved.
doi:10.1016/j.jsg.2009.09.005

dikes has been inferred on Mars from surface topographic data (Schultz et al., 2004) and, in this paper, identified there in high-resolution imaging data.

In this paper we gather and present some of the findings from recent spacecraft exploration of the solid-surface planets and satellites in our solar system (see Beatty et al. (1999) for general information on the planets and satellites in our solar system). Following current usage, terrestrial planets are bodies having solid silicate crusts and include Mercury, Venus, Earth, Earth's Moon, and Mars. Icy satellites are those whose crusts are primarily composed of ices of water, methane, and ammonia and include most of the satellites of Jupiter, Saturn, Uranus and Neptune. For brevity we refer the reader to McGill et al. (2010) for the structural geology of Venus and to Collins et al. (2010) for studies of faulting and deformation of Ganymede, Callisto, and Io. We also do not discuss the rather extensive literature on the structural geology of terrestrial impact craters (see Earth Impact Database, 2007) despite its importance to the understanding of deformation processes on the Earth and other planets (e.g., Laney and Van Schmus, 1978; Price and Cosgrove, 1990, pp. 112–118; Kriens et al., 1999; Huntoon, 2000; Kenkmann, 2002; Kenkmann et al., 2005; Pati and Reimold, 2007).

First we describe the principal types of data, such as imaging or topography, that are being used to identify and interpret planetary structures (i.e., on planets and satellites other than the Earth). Next, we present a suite of results from the geologic mapping and analysis of structures such as faults, folds, joints, and igneous dikes on bodies as diverse and complex as Mercury, the Moon, Mars, and icy satellites of Jupiter. Last, we explore two avenues that these structures can provide into the mechanics of deformation on these bodies. The overall theme of this paper is to demonstrate that structural geology should not be considered to be restricted to the Earth, and that by studying other bodies with different geodynamic styles we can learn about the response of lithospheres to a variety of stress states having different origins.

2. Data sets

Several types of data are available to permit the identification and analysis of planetary geologic structures. As discussed for example by Tanaka et al. (2010), these include imaging (using visible, near-infrared, and radar wavelengths) and topography, both having various resolutions and degrees of coverage depending on the planetary body of interest. The principal data sets currently being used in planetary structural geology are described in this section, organized by planet or satellite. Radar-based imaging systems that have been used on Venus and Titan are discussed by McGill et al. (2010) and Tanaka et al. (2010), respectively. Planetary data from NASA and European Space Agency (ESA) missions are publicly available through NASA's Planetary Data System (http://pds.jpl.nasa.gov) and its European node, Planetary Science Archive (http://www.rssd.esa.int/index.php?project=PSA).

2.1. Mercury

Until recently, the only spacecraft to observe Mercury was Mariner 10, which imaged about 45% of the planet's surface during three flybys in 1974 and 1975. Many Mariner 10 images (having an average spatial resolution of 1 km) were comparable in resolution to Earth-based telescope observations of the Moon. Currently, the MESSENGER spacecraft en-route to Mercury (Solomon et al., 2007) has completed three flybys and has returned a wealth of new imaging, topographic, and geophysical data from the planet (see Solomon et al., 2008 for some of the initial findings). Once the spacecraft enters orbit, MESSENGER's Mercury Dual Imaging System (MDIS) will provide a 250-m per pixel or better global mosaic, and the planet's topography will be measured by the Mercury Laser Altimeter (MLA) instrument and using digital elevation models derived from stereo images (Solomon et al., 2007, 2008).

2.2. Moon

Several current and forthcoming datasets will complement the high-quality imaging datasets acquired during the Apollo era of the 1960s to early 1970s (e.g., Schultz, 1976; Masursky et al., 1978) including Lunar Orbiter and Apollo metric and panoramic camera images (Tanaka et al., 2010) and images and data returned more recently by the Clementine and Lunar Prospector missions. The Lunar Reconnaissance Orbiter (LRO; Chin et al., 2007) has a suite of science instruments, two of which will be especially useful for investigating geologic structures. The Lunar Reconnaissance Orbiter Camera (LROC) is acquiring images with resolutions as high as 0.5 m/pixel, with image footprints of typically 5 $\times$ 25 km at an altitude of 50 km. The Lunar Orbiter Laser Altimeter (LOLA) is acquiring five simultaneous 5-m-diameter range measurements per shot, with an along-track shot-to-shot spacing of 25 m. Data from LROC and LOLA are expected to be useful for investigating geologic structures over a broad range of length scales.

2.3. Mars

The surface of Mars has been imaged since the flybys of Mariner 4 in 1965 and Mariners 6 and 7 in 1969, with global imaging acquired by the Mariner 9 orbiter in 1971 (see Carr, 1980, for review). The Viking 1 and 2 orbiters and landers further refined understanding of the nature of the Martian surface as well as providing an additional global dataset for the study of Martian structures (e.g., Arvidson et al., 1980). Since then many other US spacecraft, especially Mars Global Surveyor in 1999 (e.g., Smith et al., 2001), have visited the planet and acquired high-resolution imaging, spectral, and topographic data of interest to structural and tectonic studies.

The Mars Orbiter Camera (MOC) narrow-angle camera (Malin and Edgett, 2001) operated on the now inactive Mars Global Surveyor (MGS) spacecraft and provided imagery with typically 1.5–12 m/pixel. Images are typically 3 km in width and 20 km or more in length. The spatial extent and resolution of MOC imagery continues to provide information on km-scale structures in areas where higher resolution data are not yet available.

The Mars Orbiter Laser Altimeter (MOLA; Smith et al., 2001) also flew onboard MGS and gathered point altimetry of surface and cloud heights. The footprint of each range measurement is roughly 168 m in diameter, with 300 m spacing along track. Average cross-track spacing at the equator is 4 km and decreases with increasing latitude. MOLA data provide a topographic characterization of geologic structures at length scales of 5–10 km or greater. MOLA data also provide long-wavelength topographic control for higher resolution DEMs (e.g., Okubo et al., 2004).

The Thermal Emission Imaging Spectrometer (THEMIS; Christensen et al., 2004) onboard the Mars Odyssey spacecraft, while mainly intended for studies of surface composition, has accumulated sufficient imagery to provide global coverage at 19–100 m/pixel. THEMIS data are useful for investigating large-scale structures that exceed roughly 10 km in length. THEMIS data also provide insight into the distribution of dust and rock, which is necessary for discerning the morphology of bedrock structure from non-structural, surficial deposits.

The High-Resolution Imaging Science Experiment (HiRISE) camera (McEwen et al., 2007) onboard the Mars Reconnaissance Orbiter (MRO) spacecraft is currently acquiring images at up to 25–30 cm/pixel, over an image swath width of $\sim$6 km, with three-

channel color coverage within the central 20% of the image. Image length is variable and is typically 6–18 km. HiRISE imagery is well suited for studying fractures, deformation bands and other structures that have widths as narrow as 1 m and lengths of less than a few km. HiRISE color coverage is also valuable for discerning between topographic shading and variations in surface albedo due to chemical composition. Digital Elevation Models (DEMs) derived from repeat-pass stereo HiRISE imagery typically have a vertical resolution of ~1 m/pixel and provide information on the orientation of structures on the ~50 m length scale.

The Context Camera (CTX; Malin et al., 2007) also onboard the MRO spacecraft acquires images at up to 5–6 m/pixel, over a swath width of ~30 km and image length of typically more than 50 km. CTX commonly operates concurrent with HiRISE and other MRO science instruments to provide a regional synoptic context for these higher resolution data. CTX imagery is best suited for studies of geologic structures with widths greater than ~15 m and lengths of 10 km or more. DEMs derived from repeat-pass stereo CTX images typically have elevations at 20 m/pixel and provide information on the orientation of structures on the ~500 m length scale.

The High-Resolution Stereo Camera (HRSC; Jaumann et al., 2007) onboard the European-led Mars Express spacecraft is a multiple line scanner, providing color and stereo images that allow the derivation of both high-resolution digital elevation models and orthoimages (Scholten et al., 2005; Gwinner et al., 2005, 2009, in press). HRSC acquires images with a swath width on the Martian surface of typically about 60 km, which cover large areas (up to $\sim 3 \times 10^5$ km^2) with a spatial resolution of typically 12–20 m/pixel. Digital elevation models constructed from HRSC data have a grid spacing of 50–100 m, a vertical resolution of 1 m, and a vertical accuracy of ~20 m.

2.4. Outer solar system icy satellites

Voyager 1 and 2 spacecraft imagery of the late 1970s to late 1980s were useful for identifying large-scale structures on the icy moons of Jupiter, Saturn, Uranus, and Neptune. Prominent lineaments of possible structural origin were recognized on numerous icy bodies (e.g., Europa, Ganymede, Enceladus, Miranda, Ariel, Titania, Triton). Voyager 2 images remain the only datasets available for the Uranian and Neptunian moons; however, Jovian and Saturnian system science is now focused primarily on data from the Galileo (1995–2003) and Cassini-Huygens (ongoing since 2004) spacecraft.

In the Jovian system, tectonic studies of the Galilean satellites, particularly Europa and Ganymede, rely on observation of surface structure in visible-light images returned by Galileo's Solid State Imager (SSI). Images have resolutions typically of 10–100s m/pixel. Additional information about surface features and composition is provided by the spacecraft's Near-Infrared Mapping Spectrometer (NIMS) data.

In the Saturnian system, the Cassini spacecraft has produced a wealth of imagery of numerous icy moons via the Imaging Science Subsystem (ISS). This mostly visible-light camera has the capability of acquiring both wide-angle and narrow-angle imagery, the latter allowing fine details of tectonic structures (dilatant cracks, normal faults, ridges, fold belts) that can be identified, mapped, and interpreted tectonically. The thermal and compositional nature of surface materials, which provides geologic context that complements the study of geologic structures such as cracks, are also provided by the Visible and Infrared Mapping Spectrometer (VIMS) and the Composite Infrared Spectrometer (CIRS). The latter instrument was used to map temperature anomalies in the vicinity of eruptive jets from prominent cracks in the south-polar region of Enceladus. Surface structures on the Galilean satellites were also imaged during the 2007 flyby of the New Horizons spacecraft, currently en-route to Pluto, using the Long Range Reconnaissance Imager (LORRI), providing global views to augment Galileo images. The surface of Titan, which is shrouded in a thick atmosphere, has been imaged by VIMS and the Cassini Radio Detection and Ranging Instrument (RADAR), which has been used to infer topography, including the detection of mountainous regions of possible tectonic origin (Radebaugh et al., 2008, 2009). Data returned by the Descent Imager and Spectral Radiometer (DISR) of the Huygens probe provided detailed views of Titan's surface during the descent to the Huygens landing site, but are less useful for regional-scale structural geology studies.

3. Interpretation and analysis

In this section we present some of the results of recent investigations of structures on the planets and satellites, some of which are developed further in Section 4. The first step is to identify planetary landforms that can confidently be interpreted as having formed by deformation. Tanaka et al. (2010) review the main criteria for recognizing and interpreting planetary structures such as faults that are comparable to those used by field geologists and geologic mappers in their interpretation of outcrops, aerial and satellite images, and topographic data (e.g., Davison, 1994; Schultz, 1999; Peacock, 2002; Davis et al., 2005; Nemčok et al., 2005; Cunningham and Mann, 2007). The type of fault is deduced from the nature of its displacement field (e.g., Pollard and Segall, 1987), which is related to its kinematics; all three main types of faults (normal, strike-slip, and thrust) have long been recognized in planetary images of various solar system objects (see Strom, 1972; Masursky et al., 1978; Schultz, 1976; Wilhelms, 1987; Tanaka et al., 2010). Other types of structures, such as joints and deformation bands, can likewise be identified from their distinctive morphology, geometry, and topography. Folds have been recognized or inferred on several planets and satellites, both in association with subjacent faults ("wrinkle ridges"; see Schultz, 2000a and Tanaka et al., 2010 for review) and as more open, regional-scale structures (Prockter and Pappalardo, 2000; Porco et al., 2006; Okubo et al., 2008).

3.1. Mercury

Images acquired by Mariner 10 revealed a hemisphere that had undergone regional-scale horizontal contraction. Contractional deformation is indicated by landforms called lobate scarps (in the planetary literature) that are the expression of surface-breaking thrust faults (e.g., Strom et al., 1975; Dzurisin, 1978; Melosh and McKinnon, 1988; Watters et al., 1998, 2004; Watters and Nimmo, 2010). Images returned by MESSENGER are showing that lobate scarp thrust faults are globally distributed and are the dominant tectonic landform on Mercury (Solomon et al., 2008; Watters et al., 2009a).

In addition to lobate scarps discovered outside the hemisphere imaged by Mariner 10, MESSENGER revealed previously unrecognized thrust fault scarps in an area near the Mariner 10 subsolar point (see Solomon et al., 2008; Watters et al., 2009a). An example is shown in Fig. 1, where a ~270-km-long arcuate thrust fault scarp crosscuts an impact crater ~75 km in diameter (bottom arrow). The global horizontal contractional strain estimated from the cumulative length of the lobate scarps mapped in Mariner 10 images is ~0.043%, corresponding to a decrease in the radius of Mercury of approximately ~0.5 km (Watters and Nimmo, 2010). Previously unrecognized thrust fault scarps discovered in MESSENGER images indicate that this magnitude of global contractional strain (Watters et al., 1998) was underestimated (Solomon et al., 2008; Watters et al., 2009a). The additional cumulative length of all the mapped scarps in the Mariner 10 hemisphere increases the globally averaged contractional strain to 0.06%. This corresponds to a decrease in the planet's radius of ~0.7

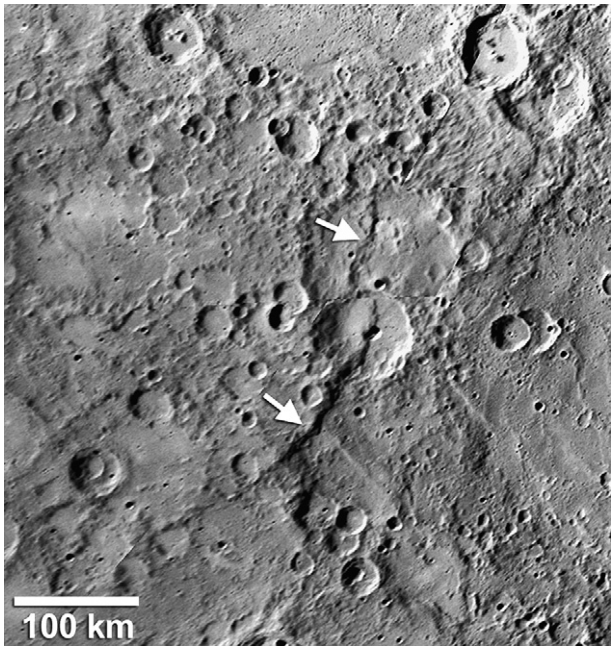

Fig. 1. Thrust faults on Mercury imaged by the MESSENGER spacecraft. A ~270-km-long arcuate thrust fault scarp crosscuts an impact crater ~75 km in diameter (bottom arrow). A second lobate scarp crosscuts a ~120-km-diameter impact crater (upper arrow). North to the top of the image.

km (Watters et al., 2009a). These updated estimates of the contractional strain and radius change are considered to be lower bounds because of the likelihood that not all lobate scarps on Mercury have been identified. The cause of global contraction is thought to be related to slow, continuous cooling of the interior and partial solidification of the Mercurian core (e.g., Hauck et al., 2004; Margot et al., 2007; Solomon et al., 2008).

In contrast to the widespread evidence of contractional deformation, normal faults that are so common elsewhere in the solar system are rare on Mercury. Evidence of extensional deformation imaged by Mariner 10 is located in the floor materials of Caloris basin, the largest, well-preserved impact basin on Mercury (Strom et al., 1975; Dzurisin, 1978; Melosh and McKinnon, 1988). The eastern portion of Caloris imaged by Mariner 10 has a series of linear and curvilinear troughs interpreted to be grabens (Watters et al., 2005; Watters and Nimmo, 2010). MESSENGER imaged the entire 1550-km-diameter Caloris basin for the first time and revealed a complex pattern of contractional and extensional deformation that post-dates basin infilling (Murchie et al., 2008; Watters et al., 2009b). Wrinkle ridges near the margin form basin-concentric and basin-radial patterns, similar to those found in Lunar mare basins. Extension in Caloris is expressed as a complex pattern of basin-radial and basin-concentric grabens. With ~98% of the surface imaged to date, grabens have been found in the interiors of three other impact basins, the ~250-km-diameter Raditladi basin, the ~715-km-diameter Rembrandt basin, and a newly discovered basin similar in size to Raditladi (Solomon et al., 2008; Watters et al., 2009b; Prockter et al., in press). The tectonic pattern in the Rembrandt basin, like Caloris, consists of basin-radial and basin-concentric wrinkle ridges and grabens (Watters et al., 2009b). Basin-radial grabens in Rembrandt, in contrast to the radial grabens of Pantheon Fossae in Caloris, are confined to a zone that extends inward from an interior ring formed by basin-concentric wrinkle ridges. Rembrandt's grabens and wrinkle ridges form a unique wheel-and-spoke pattern of tectonic landforms unlike any found in other basins of the solar system (Watters et al., 2009b). Strike-slip faults remain to be recognized on Mercury.

3.2. Earth's Moon

Tectonic landforms on Earth's Moon are largely associated with the mare basins, impact basins that were subsequently infilled by mare basalts. Most of the extensional and contractional structures (i.e., normal faults and grabens, thrust faults, and wrinkle ridges) formed on the Moon are closely related to the evolution of impact basins (Melosh, 1978; Solomon and Head, 1979, 1980; Watters and Johnson, 2010) with some contributions from global-scale tectonics related to temperature changes within the Lunar interior. In general, the pattern of tectonic landforms in a mare basin consists of basin-concentric and basin-radial wrinkle ridges in the interior and near the margin and basin-concentric grabens along the margin in the adjacent highlands. A detailed description of Lunar structures is given by Wilhelms (1987) and Tanaka et al. (2010), and their relationships to the geodynamics of the Moon are discussed in detail by Watters and Johnson (2010).

Lunar grabens are commonly linear or arcuate in planform (otherwise called straight or arcuate rilles) with a linear graben shown in Fig. 2. The normal faults that define the graben transect a pre-existing ridge where non-vertical fault dip angles are demonstrated by widening of the graben (McGill, 1971). Farther along strike, the grabens step to the left forming a relay ramp across an accommodation zone (Morley et al., 1990; Peacock and Sanderson, 1991; Davison, 1994; Crider and Pollard, 1998) with the inner faults changing polarity (dip direction) from one graben to the next.

Lunar wrinkle ridges, also referred to as mare ridges because of their association with mare basalts, are morphologically complex landforms (Strom, 1972; Bryan, 1973; Maxwell et al., 1975). Most wrinkle ridges consist of two superimposed landforms: a broad, low relief arch and a narrow, higher relief ridge (Fig. 3). These two morphologic elements can also occur independently of one another (Watters, 1988). Investigation of wrinkle ridges on the Moon and other planetary bodies including the Earth (e.g., the Yakima fold belt in Washington State; Watters, 1988) indicate that these landforms are most likely the surface expression of anticlines formed above the blind tips of subjacent reverse faults (Plescia and Golombek, 1986; Watters, 1988; Schultz, 2000a; Okubo and Schultz, 2004). The origin of wrinkle ridges and grabens associated with the Lunar mare is likely due to loading of the lithosphere by the mare basalts that induce lithospheric subsidence and flexure (Phillips et al., 1972; Melosh, 1978; Solomon and Head, 1979, 1980).

Another significant tectonic landform on the Moon that is not directly associated with mare basins is lobate scarps. Lunar lobate scarps, like their larger-scale counterparts on Mercury and Mars, are surface-breaking thrust faults that are predominantly found in

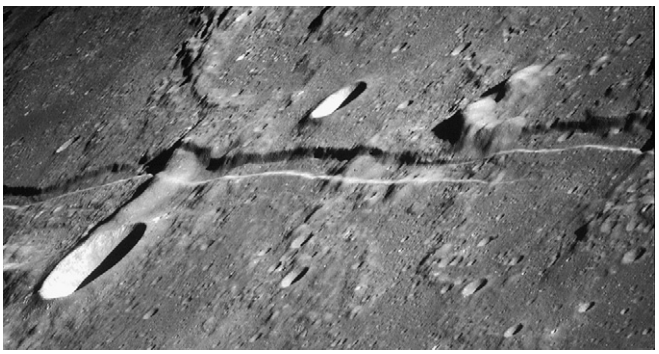

Fig. 2. Example of a Lunar graben (Rima Ariadaeus). The graben displays a change in width over the ridge in the upper left part of the image, from ~2 to ~3.5 km on the ridge crest, consistent with non-vertical fault dips, and a change in dip direction at the relay ramp (echelon stepover). Part of Apollo 10 photograph AS10–31–4645, looking toward the northwest.

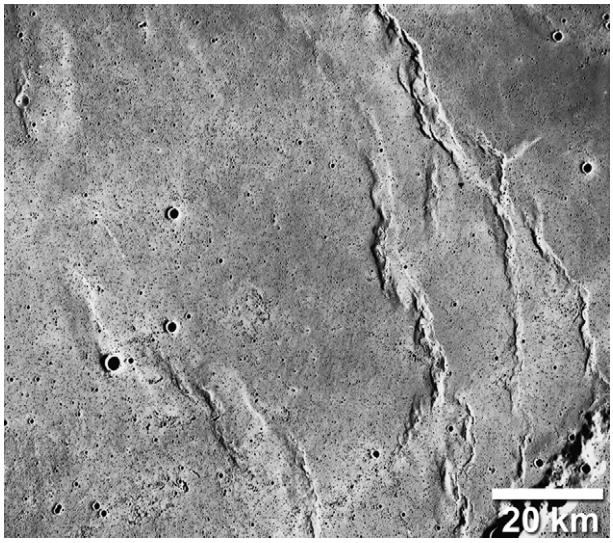

Fig. 3. Wrinkle ridge in mare basalts of Oceanus Procellarum, Moon. These thrust-fault anticlines are often comprised of two morphologic elements, a broad, low relief arch and a superposed narrow ridge (Apollo Metric Camera frame AS15-2487). North to the top of the image.

the Lunar highlands. They appear to be the dominant tectonic landform on the Lunar farside (Watters and Johnson, 2010). Lunar thrust fault scarps often occur in clusters with echelon stepping segments (Binder and Gunga, 1985; Watters and Johnson, 2010). They are apparent in high-resolution Apollo Panoramic camera images (Binder and Gunga, 1985; Watters and Johnson, 2010) and LROC narrow angle camera images (Watters et al., 2010). The absence of superimposed impact craters and their generally pristine appearance suggest a young age for the scarps (Schultz, 1976; Binder and Gunga, 1985), possibly resulting from a late-stage period of compression on the Moon (Watters and Johnson, 2010). These and other examples of Lunar structures (e.g., Schultz, 1976; Wilhelms, 1987; Watters and Johnson, 2010) continue to inform about the tectonic evolution of the Moon as the nearby Earth developed.

3.3. Mars

Mars provides a diverse and well-preserved assemblage of geologic structures. Earlier work on Martian faults and their relationships to regional and global tectonic processes is summarized by Wise et al. (1979), Tanaka et al. (1991), and Banerdt et al. (1992). A recent synthesis by Golombek and Phillips (2010) emphasizes the key roles of the ancient hemisphere-scale Tharsis volcanotectonic province (Mège and Masson, 1996; Phillips et al., 2001) and global-scale processes, including global contraction due to cooling of the Martian interior (Andrews-Hanna et al., 2008), in producing the observed structures. In the following sections we highlight recent research that illustrates Martian structural geology at regional and local scales.

3.3.1. Faulting and folding of layered sedimentary deposits

Within the equatorial region of Mars, the extensive system of canyons (also known as troughs) that collectively comprise Valles Marineris has been the subject of much study, especially with respect to its coupled structural and geologic evolution, which spans much of the planet's history (e.g., Lucchitta and Bertolini, 1989; Peulvast and Masson, 1993; Mège and Masson, 1996; Peulvast et al., 2001; Lucchitta et al., 1992, 1994; Schultz, 1998; and references therein). Key issues of current interest here center on understanding the geologic history of layered sedimentary deposits that are found at the bottom of these canyons (called chasma or chasmata (plural), from the ancient Greek language and referring to a deep, elongated, steep-sided depression (according to International Astronomical Union definitions; see http://planetarynames.wr.usgs.gov/), and characterizing the styles, extent, and timing of deformation within these deposits). Accordingly, much work has been conducted to characterize regional bedrock and deformational structure using topography derived from data sets such as HRSC (Fueten et al., 2006, 2008) and MOLA (Fueten et al., 2005). Results from these investigations have identified several locales that call for further structural mapping at yet higher resolutions in order to provide more detailed characterizations of the local structure and thereby improve current understanding of the area's geologic history.

Recent high-resolution structural mapping in the southwest Candor Chasma region of Valles Marineris (Figs. 4 and 5; Okubo et al., 2008; Okubo, in press) demonstrates how traditionally terrestrial, outcrop-scale structural mapping is now being conducted on Mars using orbiter-based imagery. West Candor Chasma is a roughly east-west trending trough that is approximately 300 km long, 140 km wide and up to 9.5 km deep. This chasma is interpreted to have formed through rifting (e.g., Schultz, 1998 and others). On-going investigations in west Candor Chasma are seeking to characterize its structural and geologic evolution, as well as the depositional environments for the layered sedimentary deposits exposed within it, and the deformational history of these sediments.

In southwest Candor Chasma, two adjacent HiRISE stereo pairs, which span a total area of approximately 18 × 20 km, are used to create two DEMs at 1 m/pixel, following the method of Kirk et al (2008). These DEMs and corresponding orthoimagery serve as the basis for high-resolution structural mapping in this part of Candor Chasma. A small portion of one of these DEMs is shown in Fig. 5. Structural orientations (i.e., bedding attitudes and strikes and dips of fault planes) are calculated from manually selected points that lie along the trace of bedding planes and other geologic discontinuities. The latitude, longitude and elevation coordinates for each point are obtained from the DEM. Roughly 5–10 points are defined for each discontinuity over trace lengths of 50–100 m. The best-fit plane to each set of points is then determined using a multi-linear regression routine, and a correlation coefficient better than 0.98 is typically achieved. Thus structural orientations are effectively resolved at length scales on the order of ~75 m. Validation testing also shows that ~50–100 m is in general a reliable length scale for repeatable measurements of structural attitudes in this location and for these specific DEMs. Measurements of structural attitudes at shorter length scales are hindered by high-frequency topography, which

Fig. 4. Perspective computer-generated view of layered sedimentary deposits in west Candor Chasma. These rocks are deformed by a series of km-scale thrust faults and related folds (cf. Okubo et al., 2008; Okubo, in press). The image is a HiRISE color composite (Delamere et al., 2010) from PSP_ 003540_1735 overlain on a 1 m/pixel DEM, with no vertical exaggeration. The lower edge of the image is ~750 m wide. The view is from a simulated altitude of 250 m above the ground surface looking toward the northeast.

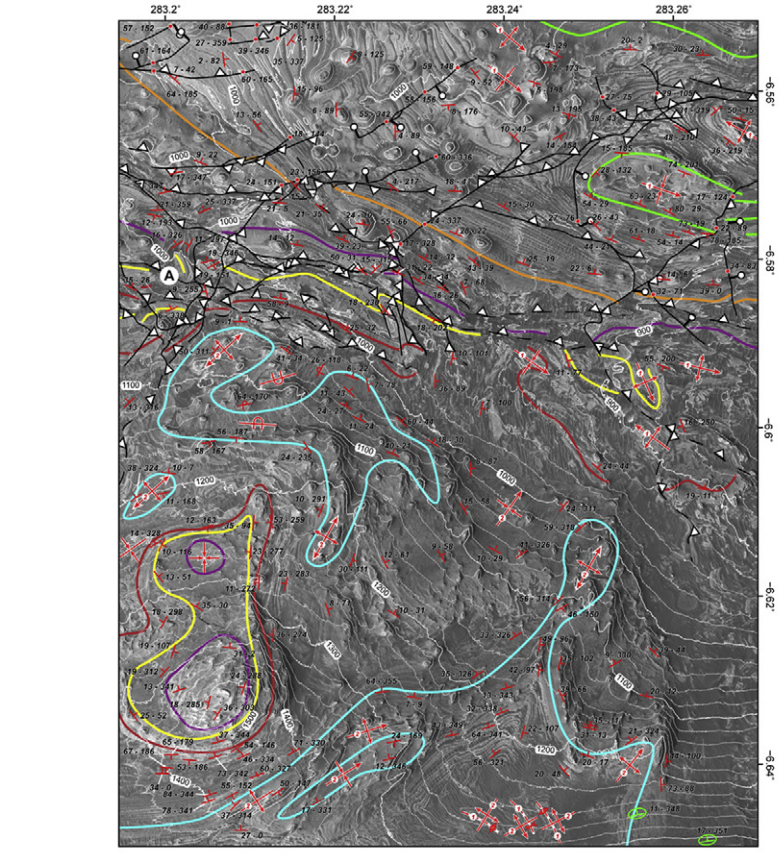

Syncline. Arrowhead along major axis is plunge direction. Number is the interpreted stage of folding.

Anticline. Arrowhead along major axis is plunge direction. Number is the interpreted stage of folding.

Monocline. Arrowhead along minor axis is dip direction, arrowhead along major axis is plunge direction. Number is the interpreted stage of folding.

Anticline with overturned limb. Arrowheads along minor axis point down dip, arrowhead along major axis is plunge direction. Number is the interpreted stage of folding.

Syncline with overturned limb. Arrowheads along minor axis point down dip, arrowhead along major axis is plunge direction. Number is the interpreted stage of folding.

Superimposed syncline. This is the oldest of a pair of superimposed folds. Number is the interpreted stage of folding.

Superimposed anticline. This is the oldest of a pair of superimposed folds. Number is the interpreted stage of folding.

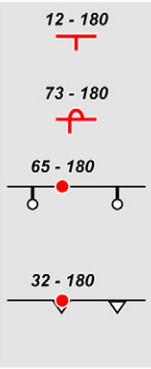

Strike and dip of bedding. First number is dip, second number is dip direction.

Strike and dip of overturned bedding. First number is dip, second nu

Normal fault. Bar and ball on hanging wall. Dot shows location of fault plane strike and dip, first number is dip, second number is dip direction.

Thrust fault. Barb on hanging wall. Dot shows location of fault plane strike and dip, first number is dip, second number is dip direction.

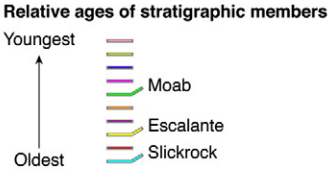

DTM based on PSP_003540_1735 and PSP_003474_1736.
Vertical datum is the lowest elevation in the DTM.
Height contours are in meters.
Basemap is PSP_003474_1735.

Fig. 5. Subsection of a structural geologic map from west Candor Chasma, Mars. Orientations of bedding and fractures are measured from a corresponding 1 m/pixel DEM (cf. Okubo et al., 2008; Okubo, in press). Thrust faults are prominent in this area, resulting in fault-bounded blocks and occasional exposures of repeated stratigraphy (e.g., area surrounding point A). Lines designate ~100-m-thick marker layers. Map is superimposed on HiRISE image PSP_ 003540_1735, with illumination from the upper left. Map area is approximately 4.5 km wide.

may be due to boulders, sand dunes, and variability in the planarity of the discontinuities.

Faults and folds have been observed in these layered deposits since early imaging by MOC, but their characteristics and significance has remained ambiguous. By using high-resolution imagery and DEMs, the sense of displacement and geologic history of these structures can now be determined. The sense of slip along these faults is established from both the apparent offset and measured orientations of crosscut bedding and other discontinuities. Faults in this area are found to have either thrust or normal displacement senses (Figs. 5 and 6). The thrust faults have an average dip angle of $31^\circ \pm 11^\circ$, whereas normal faults have an average dip angle of $55^\circ \pm 11^\circ$.

Thrust faults form networks of linked and mutually crosscutting faults that are commonly manifest as zones of thrust-bounded fault blocks. Thrust faulting has also resulted in repeated stratigraphic sequences in some areas (Fig. 5). While there is considerable scatter in the measured fault orientations, the maximum horizontal contraction accommodated by thrust faulting is found to have a roughly north–south orientation as evident from stereonet analysis (Fig. 6).

Normal faults are observed in isolated, linked, conjugate and graben-bounding geometries. These faults are mutually crosscutting, but rarely intersect along strike as the thrust faults commonly do. The maximum observed length for a normal fault in this area is 1.6 km. Fault throws have not yet been determined. Given the orientations of these normal faults (Fig. 6), horizontal extension occurred in the N60°E and S30°E directions.

Measurements of true thickness for individual layers are calculated from apparent thickness as measured in the map-projected HiRISE image and the dip of the layers in areas where these layers are not faulted. The majority of the layers are found to be $\sim$5 m thick. Interspersed amongst these thinner layers are massive to weakly bedded layers that are generally $\sim$100 m thick (Fig. 5). The 100 m thick layers are traceable for several 10's of km to the east and west of the study area and provide useful marker beds for regional structural interpretations.

Bedding within these sedimentary deposits is found to generally dip toward the center of west Candor Chasma in areas where these beds are not adjacent to prominent faults or folds (Fig. 6). This orientation of bedding is consistent with deposition of these sediments within a pre-existing or actively subsiding basin. One difficulty with these sediments being deposited in an actively subsiding basin, however, is that normal faults that can be attributed to subsidence of the chasma are not observed and there is no evidence of syn-depositional deformation. Thus deposition of these sediments in a pre-existing basin is most consistent with the observations.

The entire stratigraphic sequence of sedimentary deposits exposed in this area appears to be conformable, with the exception of the occasional zones of thrust fault-bounded blocks. This allows for the thickness of the exposed stratigraphic section to be estimated. Measured bedding orientations are used to correct for geometric distortion of apparent layer thicknesses due to dip, and these deposits are found to constitute a roughly 3.5 km thick stratigraphic section. This estimate has not yet been corrected for stratigraphic duplication due to faulting because calculations of strain across individual faults are currently ongoing. Fault duplication of stratigraphy is however currently estimated to contribute less than 200 m to the apparent section thickness, given that most of these faults are less than a kilometer in length and therefore have correspondingly small (meter-scale) displacements.

Numerous synclines and anticlines are identified throughout the area. Where not near an adjacent fault, the majority of the folds are shallowly plunging ($<\sim 10^\circ$) and trend roughly S60°E,

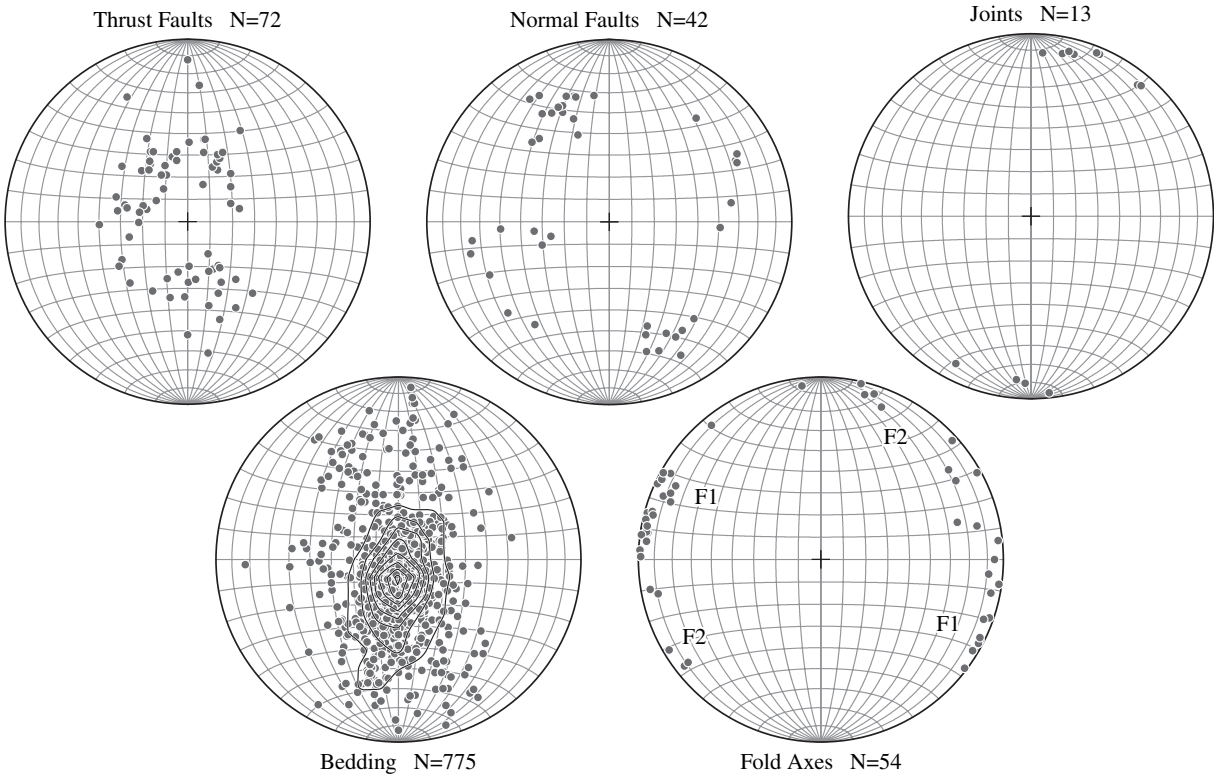

Fig. 6. Orientations of measured fractures, folds and bedding (given by their poles) from ongoing structural mapping in west Candor Chasma, Mars. The plot of bedding orientations is contoured at intervals of 2% per 1% area. Superposition relationships are used to determine the sequence of deformation for the plotted population of folds (F1 = first, F2 = second; points indicate trends and plunges of fold axes). All plots utilize the Schmidt equal area projection, lower hemisphere.

indicating a maximum principal contractional strain oriented at ~N30°E (Fig. 6). A second, less populous, set of folds is also identified. These folds are again shallowly plunging (<~10°–20°) and trend roughly N55°E. This second set of folds corresponds to a maximum principal contractional strain direction of ~S35°E. These two populations of folds are superimposed in some areas, which provides insight into their relative ages. The folds exhibit the classic concordant–discordant, dome, basin, crescent and mushroom interference patterns (cf. Ramsay and Huber, 1987; a few examples are visible at the south end of Fig. 5). These superposition relationships indicate that the S60°E-trending folds are older (F1) and overprinted by the younger N55°E-trending folds (F2). This sequence is consistent for all superimposed folds that have been identified to date and indicates a roughly 65° counter-clockwise rotation in apparent horizontal shortening between the first and second folding event.

Folds are also being discovered adjacent to some of the longer thrust faults. The long axes of these folds generally parallel the trend of the adjacent fault, and these structures appear to be fault propagation folds. Mapping and characterization of these fault-cored folds (examples in Fig. 4) is ongoing at the time of this writing.

Where crosscutting relationships are observed, there is a general pattern of relative age amongst the faults and folds. The F1 folds are generally the oldest deformational structures observed in this area, followed in age by the normal and thrust faults. While not all faults and folds have unambiguous crosscutting relationships, these relative ages hold true in all clear instances. Additionally, the thrust faults generally crosscut the normal faults, however crosscutting relationships are insufficient to establish the relative ages of all intersecting faults. Crosscutting relationships between faulting and the F2 folds are not clearly observed.

These results provide new insight into the depositional setting of the local sedimentary rocks and structural evolution of this part of Candor Chasma (Okubo et al., 2008; Okubo, in press). An important finding is that at least some of the layered sediments exposed within west Candor Chasma were deposited after the chasma had formed. This means that local sedimentation processes persisted after cessation of activity of chasma-related rifting in this area. Further, this implies that faults and folds observed within these younger sedimentary rocks are not direct evidence of the normal faulting that created this chasma. Instead, multiple episodes of local gravity-driven slumping of these sediments are the currently favored explanation for the observed strain (Okubo et al., 2008; Okubo, in press). Work is currently underway to investigate the effects the observed deformational structures would have exerted on the migration of paleo-groundwater through these deposits (e.g., Okubo et al., 2009) which is important given the growing body of evidence for groundwater activity in this and other areas in the Martian past (e.g., Grotzinger et al., 2005; Squyres et al., 2006; Andrews-Hanna et al., 2007; Harrison and Grimm, 2009).

Angles of fault dip provide insight into the mechanical properties of these sedimentary rocks. Given that the faults in this area are found to generally post-date the majority of the folds, the observed magnitudes of fault dip are regarded to be largely representative of dip of the fault as it propagated. Thus measurements of fault dip can be used to estimate the angle of internal friction, φ_f, of these layered deposits. Assuming that these faults propagated along planes that are optimally oriented for Coulomb slip, fault orientation is a function of φ_f through

$$\theta_f = 45^\circ + \frac{\phi_f}{2} \quad (1)$$

(Jaeger and Cook, 1979), with θ_f being the angle between the maximum compressive principal stress direction and the normal to the optimally-oriented plane for frictional slip. Holding lithostatic load as the vertical principal stress in an Andersonian stress state for faulting (Anderson, 1951), the angle of θ_f becomes equivalent to the dip of the optimally-oriented fault plane, θ_{dip}, for normal faults. For thrust faults, θ_f is the complementary angle to θ_{dip}.

Through Eq. (1), a median friction angle of $31^\circ \pm 14^\circ$, is calculated for the angles of fault dip measured in southwest Candor Chasma. These median values are generally larger than previous estimates of ~5°–18° for layered deposits elsewhere in Valles Marineris gathered from back-calculations of slope failures (Schultz, 2002), although a more detailed slope-stability analysis that incorporates dynamic seismic loading and groundwater confirms failure of layered deposits having friction angles of ~18° (Neuffer and Schultz, 2006). The angles of friction for the faults discussed here, that are not related to slope instability, are consistent however with laboratory measurements of intact rock (e.g., Byerlee, 1978), as well as moderately weathered and fractured rock masses (e.g., Hoek and Brown, 1997). Eight of the 57 fault dip measurements are found to be incongruous with the above assumptions because they were either less than 45° for normal faults, or greater than 45° for thrust faults. These measurements are excluded from the above statistics and may be due to stress interactions with adjacent faults or slipping bedding planes (e.g., Roering et al., 1997; Okubo and Schultz, 2006b).

3.4. Faulting at Tempe Terra

Fault linkage is an essential process in the growth of fault populations (e.g., Crider and Pollard, 1998; Trudgill and Cartwright, 1994; Peacock, 2002). Fault populations on Mars display evidence for linkage via relay ramps (Fig. 7). Until recently, however, the spatial resolution of topographic data was insufficient to resolve the detailed three-dimensional properties of relay ramps. This situation changed with the availability of high-resolution digital elevation models. It can now be demonstrated quantitatively how the offset along faults varies toward the fault tips, where a relay ramp marks the transition from one fault segment to another one. An example is given in Fig. 8, which shows part of the Tempe Fossae rift in northeastern Tharsis (Hauber and Kronberg, 2001; Wilkins et al., 2002). Individual rift basins are bounded by fault scarps that show clear evidence for linkage at breached relay ramps, a situation that is also typical for other Martian rifts (Hauber and Kronberg, 2005; Grott et al., 2005; Kronberg et al., 2007; Hauber et al., in press). Topographic profiles across the fault scarps show how the vertical offset at the two linked fault segments decreases over a distance of ~15 km from values of ~500 m to zero at the fault tips at the relay ramp. The profiles also reveal that the cross-sectional geometry of

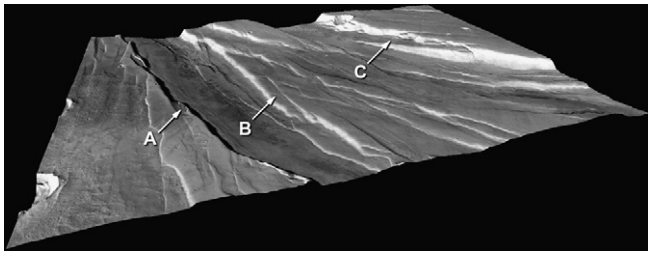

Fig. 7. Perspective view of the southeastern segment of the Tempe Fossae rift, Mars (Hauber and Kronberg, 2001) (image center at 39.85°N, 284.75°E; image and topography from HRSC orbit h1495_0000; view toward northwest; illumination from left/south; image dimension 75 × 100 km). Linkage of fault segments is visible at different scales, from small ("A") to large ("C").

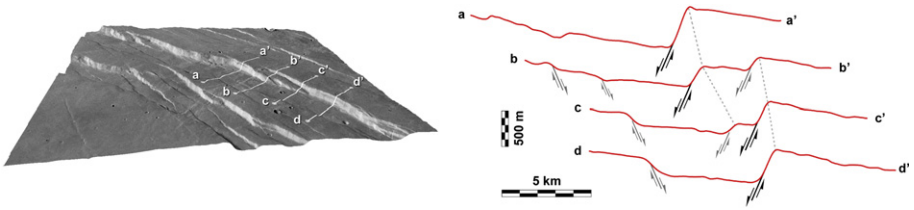

Fig. 8. Fault segmentation and linkage on Mars. (a) Perspective view of a series of grabens cutting the northwestern flank of Alba Patera (image center at 44.8°N and 247.9°E; image and topography from HRSC orbit h1272_0000; view toward west; sun illumination from left/south; image dimension 55 × 62.5 km). The faults bordering the grabens are segmented, and breached relay ramps link individual fault segments. (b) The profiles a–d sample the transition from one prominent fault segment in the southwest over a relay ramp to another fault segment in the northeast. The offset across one fault segment decreases in the relay ramp, while the offset across the other fault segment correspondingly increases.

the rift graben is not symmetrical. One bounding or border fault (in this case, the northwestern one) is much more pronounced than the other one, and the graben floor is clearly tilted, although the regional topography does not display any tilting. This geometry is typical for terrestrial grabens such as the Canyonlands graben system (e.g., Trudgill and Cartwright, 1994; Moore and Schultz, 1999; Schultz et al., 2007).

The limited spatial resolution of early data sets (Viking Orbiter images with typical resolutions of 60–100 m/pixel) hindered the detailed structural analysis of Martian grabens. Many narrow grabens were considered to be "simple" (i.e., symmetrical in cross section and bounded by two parallel single normal faults; e.g., Tanaka et al., 1991; Banerdt et al., 1992). With the availability of higher resolution topographic data, it is possible to investigate the structure of Martian grabens in unprecedented detail. It is now apparent that previously supposed simple grabens are neither simple nor symmetric. To highlight the potential of new high-resolution data in the structural analysis of Martian faults, we investigate a graben on the northeastern flank of Alba Patera (Cailleau et al., 2003) (Fig. 9). The depth of the graben is not uniform along its length. Instead, the largest depth (which on Earth is commonly the area of a depocenter) is located at the graben center and shifted toward the eastern border fault (Fig. 9a). This is also typical for terrestrial grabens where it approximately mirrors the location of the maximum uplift on the adjacent footwall (cf. Fig. 15.7a in Schultz et al., 2007).

Inspection of high-resolution images reveals that the bounding faults of the graben are not composed of one single normal fault but consist of several individual fault segments that are arranged in echelon patterns (Fig. 9b). In the zone of overlap, relay ramps, which may be breached, accommodate the transition of the throw from one fault to the adjacent one. The linked fault segments constitute the border fault system that, if observed at lower spatial resolution, would resemble a single long normal fault.

The mechanical effects of fault linkage become evident if displacement profiles are constructed along the border fault systems (Fig. 10) by measuring the vertical offset (the throw) across the border fault at many individual positions (Fig. 9c). The aggregate displacement profile (taken here to be proportional to the throw profile) of the western border fault system (Fig. 10a) exhibits the characteristics of the displacement (throw) profiles of individual unlinked faults (Barnett et al., 1987; see Peacock and Sanderson, 1991 for terrestrial examples of displacement profiles of linked faults), i.e., a continuous increase of displacement from the fault tips toward the area of maximum displacement (or throw), which is located at or near the fault's midpoint. The shape of the aggregate displacement profile is in agreement with results from fieldwork and theoretical research, which suggest semi-elliptical or triangular displacement profiles (see Manighetti et al., 2005, and references therein).

The eastern border fault system displays a more complicated pattern. The northern half of it shows displacements that are increasing continuously and almost linearly toward the midpoint of the graben. The aggregate displacement profile also shows that the cumulative displacement at a relay ramp between fault segments c–c' and d–d' (Fig. 10b) follows the trend of the continuous displacement increase toward the graben center. The southern part of the displacement profile of the eastern border fault system is characterized by a flat-topped curve. This might be attributed to the effect of a nearby and parallel smaller graben (Fig. 9b), i.e., the displacement is transferred between stepping faults.

Statistical analysis of fault populations can provide insight into the mechanical properties of the faulted volume, i.e., about the different mechanical properties of layers in a stratigraphic sequence (e.g., Soliva and Schultz, 2008; Polit et al., 2009). Histograms of cumulative frequency of fault length distributions may be approximated by power-law or exponential functions (e.g., Ackermann et al., 2001). Faults that affect vertically unconfined rock volumes (thick-skinned tectonics) exhibit a power-law behavior, reflecting the self-similar geometry of faults (with linear displacement-length scaling; Schultz and Fossen, 2002; Soliva et al., 2005). On the other hand, the displacement-length relationship of faults affecting a brittle rock layer with a limited thickness is scale-dependent, and can be fitted with exponential functions (Soliva and Schultz, 2008).

New image data provide both high spatial resolution and wide coverage that facilitate the mapping of fault populations (Fig. 9d). The cumulative length-frequency plot of 473 mapped faults (Fig. 11) displays a characteristic tri-segment shape (Mansfield and Cartwright, 2001). Similarly shaped plots were shown for Martian faults on global (Knapmeyer et al., 2006) and local scales (Schultz, 2000b; Hauber et al., 2007). The fault population shown here (Fig. 11) can be approximated by a power-law fit in the length range between ~2 and 10 km (faults shorter than 2 km were not considered in the analysis due to truncation effects), consistent with faults that are unrestricted at depth. The examples show how detailed analysis of structural features benefits from the availability of recently acquired high-resolution images and topographic data sets, as also illustrated by the results for stratigraphically restricted normal faults (e.g., Soliva et al., 2005) recently demonstrated for Mars by Polit et al. (2009).

High-resolution mapping in west Candor Chasma demonstrates how current Mars data sets are sufficiently detailed to enable outcrop-scale investigations into a local area's structural evolution and geologic history. These data enable measurements of the orientations of faults and other fractures, bedding, and fold axes at the 50–100 m scale that, in conjunction with additional observations such as crosscutting relationships and displacement distributions along fractures, yield new insight into the mechanics and evolution of tectonic processes, as can be appreciated as well from the detailed observations and measurements of Martian normal fault and graben sets. These analyses help to elucidate more details of the underlying processes and tie together earlier structural and

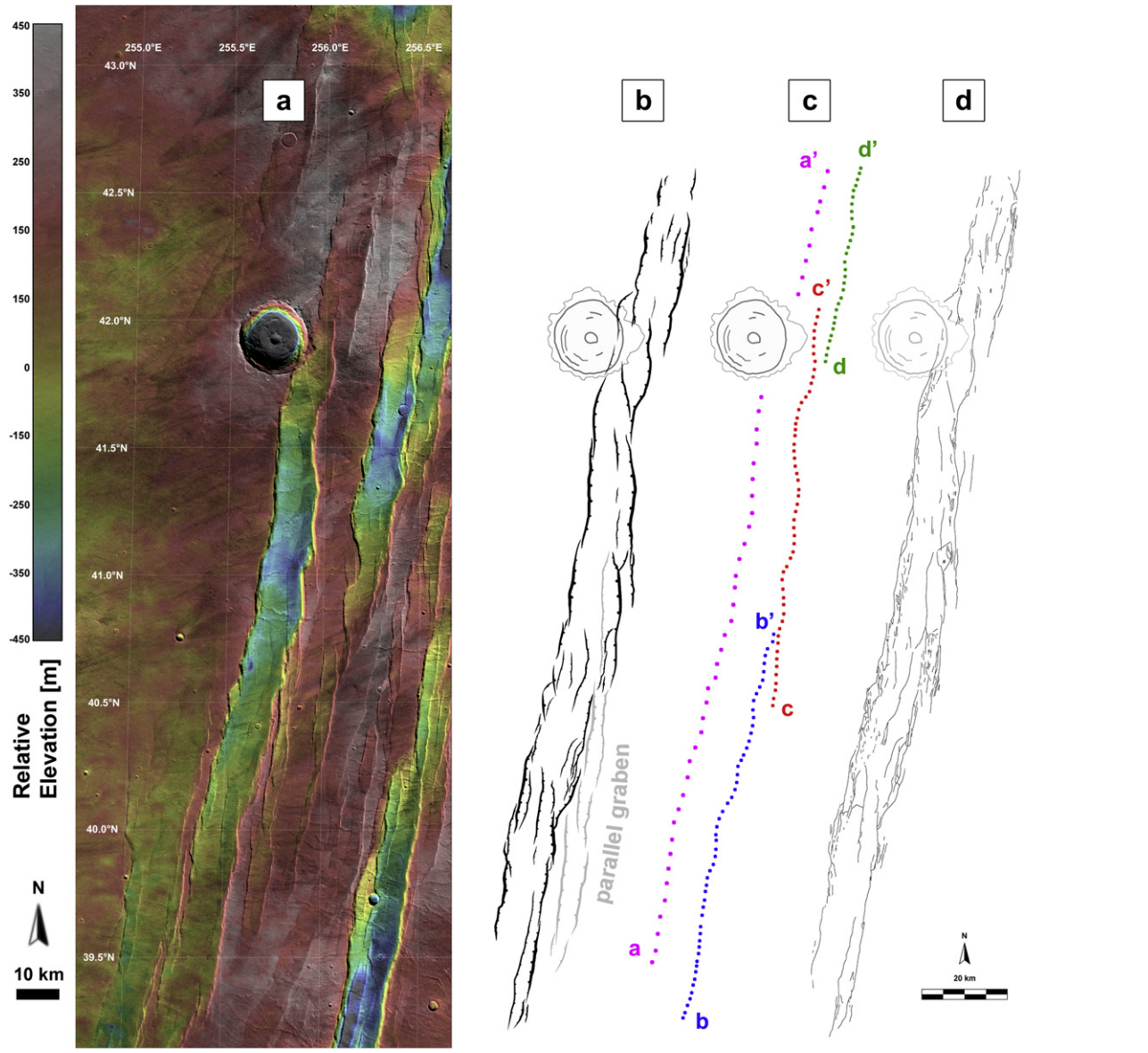

Fig. 9. Structure of a NNE-SSW-trending graben on the northeastern flank of Alba Patera, Mars. (a) Topographic image map with constant regional slope removed (i.e., colors as indicated by the color scale bar are relative elevations). The deepest area is located approximately halfway along the total graben length (image and topographic data from HRSC image h0068_0009). (b) Schematic tectonic map, showing the segmentation and echelon arrangement of the border fault systems (i.e., the eastern one). A smaller graben (light gray shading) with a more northerly trend is situated close to the main graben at its southeastern part. (c) Positions where the vertical offset across the border fault systems have been measured in HRSC DEM. The colors correspond to the colors of the (border) fault displacement profiles shown in Fig. 10. (d) Map of 473 individual faults mapped in a HRSC orthoimages with 25 m/pixel resolution (see Fig. 11 for a plot of the fault length distribution). Map scale and projection are the same for panels a–d.

tectonic interpretations made using previous, lower-resolution datasets. In west Candor Chasma specifically, such investigations have helped to show that sedimentation within the chasma continued to occur well after chasma-related rifting had ceased and that much of the deformation in these post-chasma sediments are likely due to endogenic processes such as landsliding. The high-quality imaging and topographic information now available for faults from Mars and elsewhere demonstrates the operation of common processes that govern the growth, segmentation, interaction, and linkage of faults on the Earth and other planetary bodies.

3.5. Icy satellites

The identification of structural landforms on icy satellites utilizes kinematic analysis techniques (e.g., offset indicators), augmented by remote sensing of surface characteristics and geometries. Unlike Mars or Earth, digital elevation models are only available for small areas on the icy satellites, with topographic information being obtained primarily through point photoclinometric and stereographic techniques on these bodies. Nimmo and Schenk (2006) used this technique on Europa to identify a normal fault scarp that was too subtle to easily identify in surface imagery. Digital elevation models created from stereo images have recently been used to investigate graben geometries and to infer properties of lithospheric thicknesses of icy satellites (Giese et al., 2006, 2008). Surface albedo is another diagnostic tool, as exposed normal fault scarps in ice tend to have a higher albedo than the rough upper surfaces of the tilted blocks between the fault scarps (e.g., Europa, Ganymede, Dione). The faults may also display segmentation along their lengths, echelon patterns that imply

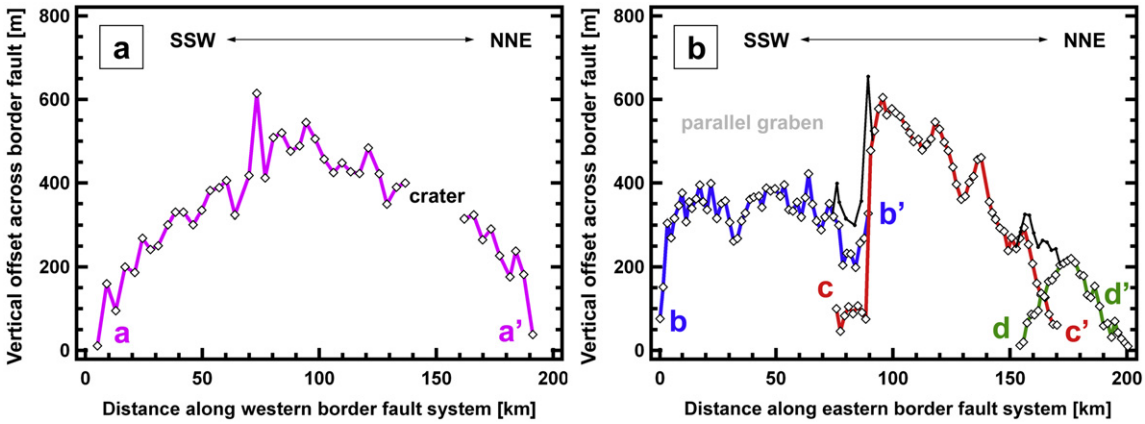

Fig. 10. Throw profiles along the border fault systems of the graben shown in Fig. 9. The locations where the profile measurements (open squares) were taken are marked in Fig. 9c. (a) Western border fault system. The profile shows an approximately symmetric distribution of displacements, with throws continuously increasing from the graben ends and the maximum displacement (throw) located halfway along the graben. Although the western border fault system is segmented into individual faults that are linked via relay ramps, the aggregate displacement profile resembles that of a single large fault, thus demonstrating the mechanical effects of fault linkage. (b) Eastern border fault system. Three large individual faults were measured and the aggregate throw profiles at the overlapping zones are indicated by black lines. In the northern part of the eastern border fault system (Fig. 9c and d), the displacements continuously increase from the graben end toward the center of the graben, and the two fault segments are mechanically linked. In the southern part (Fig. 9b), the displacement profile is flat-topped. We interpret this to be an effect of the paralleling smaller graben (see Fig. 9b) and the associated shear stress perturbation around it. Throw minima (e.g., of fault c, marked in red) represent linkage sites.

oblique offsets, and variations in scarp height (Collins et al., 1998; Kattenhorn, 2002; Goff-Pochat and Collins, 2009), analogous to normal faults on Earth and Mars.

Voyager spacecraft images were useful for identifying large displacements along structures such as strike-slip faults on Europa (Schenk and McKinnon, 1989). Since then, Galileo imagery allows kinematic indicators to be more readily identified. For example, dilational pull-apart structures on Europa, called dilational bands (Prockter et al., 2002; Kattenhorn and Hurford, 2009), formed by cracking of the ice shell and subsequent infilling of the dilational gap by warm, buoyant ice rising up from below. The band margins can be reconstructed geometrically by matching piercing points defined by older features cut by the band (Fig. 12a). Lateral offsets associated with strike-slip faults can also be measured directly based on matching features to either side of the fault (Fig. 12b).

In many cases, however, motions along lineaments on Europa can be difficult to interpret. The time-variability of the Europan stress field (see Section 4.1) results in complex kinematics along fractures in the ice shell. Combinations of dilation and shearing on icy satellites can be directly observed in spacecraft images; however, contraction across a lineament can produce apparent offsets that superficially resemble strike-slip fault offsets (Fig. 13a), implying that lateral offsets are not necessarily diagnostic of strike-slip activity. Lateral offsets are commonly observed along linear landforms called ridges that exhibit raised edifices of ice to either side of a central crack. Hence, ridge development may be related to the kinematic history along the central crack, whether dilational, contractional, or involving shearing, with such motions gradually

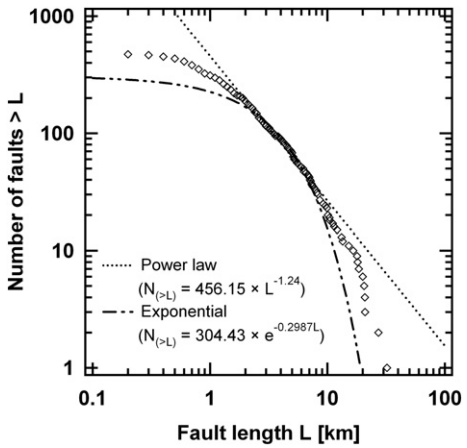

Fig. 11. Cumulative length distribution of all mapped faults shown in Fig. 9d. Best fits are shown for power-law and exponential functions (fit functions labeled on graph). A length truncation limit (lower bias) of 2 km was applied, following the considerations of Soliva and Schultz (2008) and applying them to the HRSC data set with a map-projected image resolution of 25 m/pixel. No censoring effect (upper bias) was considered, since the mapping window was large with respect to the mapped grabens. Neither a power-law nor an exponential function can be fitted to the full range of the data (2–32 km).

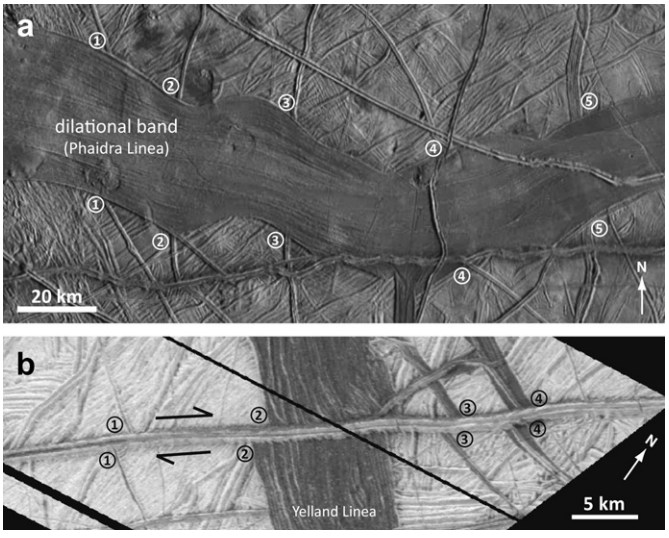

Fig. 12. Use of piercing points to reconstruct motions along Europan lineaments. (a) Five examples (numbered) of matching features to either side of a younger dilational band informally called Phaidra Linea. Several crosscutting features (cracks and ridges) are younger than the band (from Galileo mosaic 11ESREGMAP01). (b) Four examples of offset features along a right-lateral fault on Europa. The offset features include relatively older ridges (feature 1) and dilational bands (features 2–4). The dark dilational band cut by the fault at the center of the frame (feature 2) is Yelland Linea (from Galileo mosaic 12ESWEDGE_03).

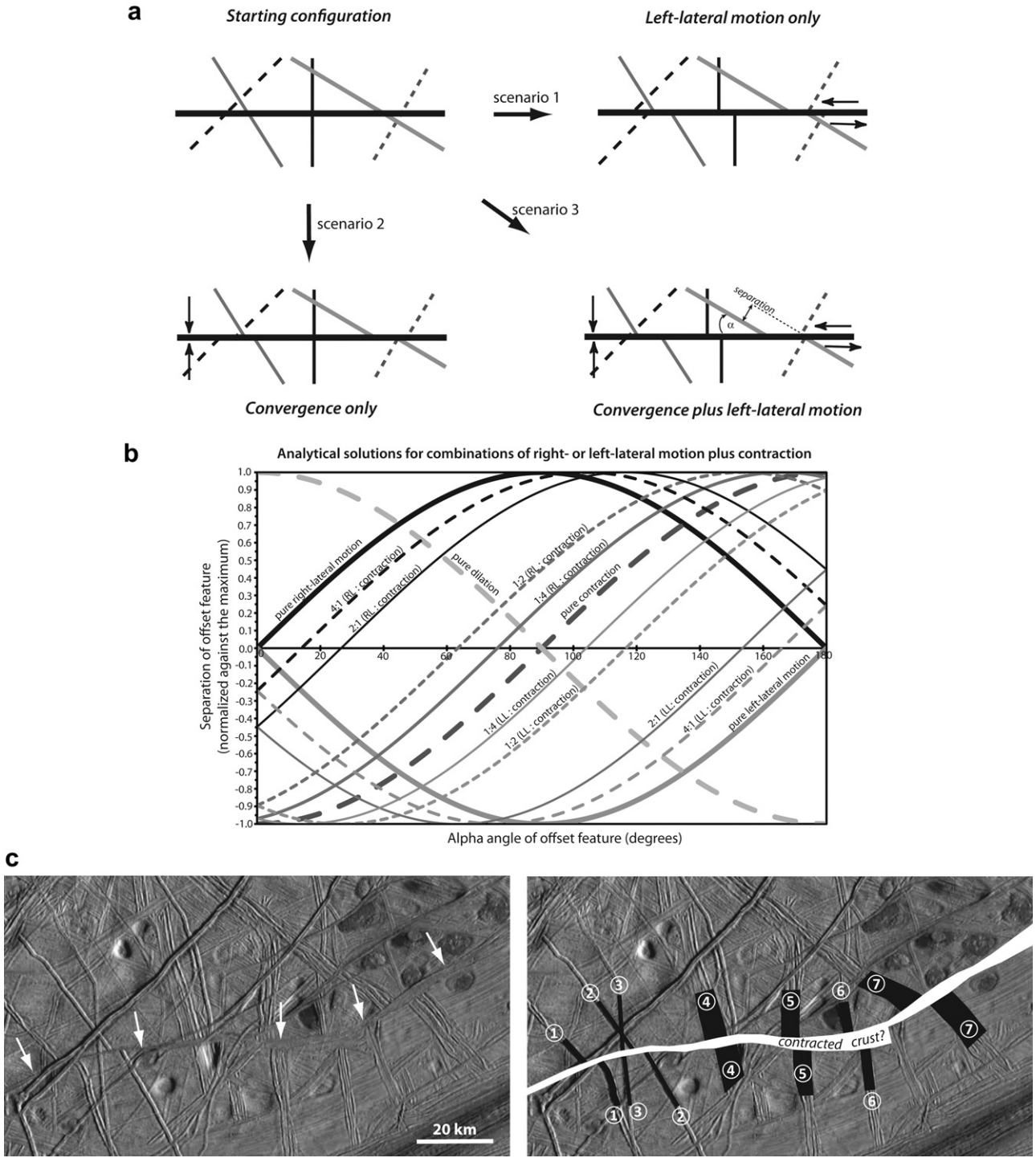

Fig. 13. Creation of apparent lateral offsets through convergence along Europan lineaments. (a) Three hypothetical scenarios involving left-lateral offset, convergence, or a combination thereof. Feature orientations are defined by angle α (measured clockwise, as in the bottom right example), whereas offsets are characterized using the separation. Mirror-image scenarios exist for right-lateral offset. (b) A family of analytical curves showing the effect of angle α on normalized separations for a number of kinematic scenarios involving lateral offsets plus convergence. A set of curves can also be produced for dilation plus lateral offsets. (c) Example of a possible site of contraction on Europa (white arrows in left image) (from Galileo mosaic 15ESREGMAP01). Apparent offsets of seven older features (numbered black lines in right image) imply contraction plus a small component of left-lateral offset within a localized zone of deformation (white region).

constructing the ramparts to either side of the crack through associated processes such as extrusion, buoyant warping, or buckling (Kattenhorn and Hurford, 2009).

Contractional structures are sparse on Europa despite the prevalence of extension in the ice shell that far exceeds plausible estimates for the surface area increase caused by ice shell thickening, implying that the manifestation of contraction may not have been fully identified. A kinematic analysis of lineaments that show apparent lateral offsets is possible by comparing the amount of normalized separation between relatively offset features relative to

the angular relationship, α, between the lineament and its offset features (Fig. 13b). For example, one band-like structure in the northern trailing hemisphere (the side of the moon facing opposite to the direction of orbital motion for the case of a moon in a synchronous orbit) (Fig. 13c) appears to have undergone contraction and a small amount of left-lateral strike-slip offset (although the ratio is variable along strike). Such analyses allow any contractional component of the kinematics to be identified graphically, potentially leading to more refined estimates of contractional strains associated with brittle tectonics of the ice shell.

4. Applications

The type of planetary geologic structure is determined by a variety of criteria (Tanaka et al., 2010) including morphology, topography, and relationships with surrounding stratigraphic units. These structures then permit the formulation and testing of mechanical or geodynamic models for crustal deformation including changes in rotation rate (despinning or spin-up), rotation axis (reorientation or true polar wander), plate or stagnant-lid tectonics, impact basin-related vertical movements, or global contraction. Many of these processes that are distinct from Earth-like plate tectonics are described by Watters and Nimmo (2010) and Collins et al. (2010). In this section we show how structures are being used to test and refine mechanical models of crustal deformation at a variety of scales.

4.1. Relationship between faults and causative stresses on icy satellites

Mechanical analyses of the icy satellites of the Jovian planets present unique challenges compared to terrestrial structural analysis. On Earth and other terrestrial planets, mechanical analyses typically involve unraveling a history of stress orientations in a region of study based on the structures observed. The relationships between stress and the resultant deformation structures are examined in the context of physically based criteria for brittle failure, such as the Coulomb or Griffith failure criteria. Observations of different types, orientations, and ages of structural features thus allow a stress history to be inferred, which can then be placed into the context of a tectonic history. A fundamental characteristic of such studies is that the remote, or far-field, stresses are typically slowly varying, resulting in discrete episodes of deformation. Stresses on the terrestrial planets are ultimately related to processes that are long-lived and change over time periods of perhaps millions of years (e.g., tectonic plate motions on Earth). Mechanical models thus commonly utilize a static approach, in which far-field stresses are assumed to be relatively constant during a deformation event (see discussion of regional vs. fault strain rates by Cowie et al., 2007).

In contrast, the stresses driving deformation in some icy satellites are typically not related to plate motions or endogenic processes but are instead a response to body forces created by the gravitational pull of the parent planet (see Collins et al., 2010 for a review). For a moon locked into a synchronous, circular orbit (e.g., Triton), there are no daily changes in the nature of the gravitational forces as the moon orbits its parent planet, resulting in no tidal driving mechanism for ongoing deformation. However, many icy satellites occupy eccentric orbits, such as Europa (having an orbital eccentricity, $e \approx 0.01$), Enceladus ($e \approx 0.005$), and Dione ($e \approx 0.002$). For satellites close to their parent planets (e.g., Europa, Enceladus), these orbits result in diurnal components of the stress field that are continuously varying.

The repeated changes in satellite shape during the course of a single orbit (the diurnal cycle) result in a continuously varying stress state (Greenberg et al., 2003). Dilatant cracks on some icy moons appear to reflect these changing stress conditions. Structures called cycloids have been described on Europa (Hoppa et al., 1999b; Marshall and Kattenhorn, 2005) that form arcuate segments linked at sharp cusps (Fig. 14), with each arc of a cycloid chain hypothesized to have grown during a single orbital cycle. Although the stresses rotate by 180° during the diurnal cycle, they are only large enough to exceed the tensile strength of ice during a portion of the orbit, resulting in arc lengths of less than 180°. The resulting cycloid crack does not grow as the stresses continue to rotate through the remainder of the orbit. Once the tensile strength of the ice is again exceeded during a subsequent orbit, crack growth continues in a new direction, perpendicular to the new least principal stress orientation, resulting in a cusp (analogous to a kink along terrestrial joints) at the intersection of the older and the newer cycloid crack segment. The formation of this cusp is also related to the effects of shearing and dilation at the tip of the arrested cycloid crack as the tidal stresses rotate. For example, Groenleer and Kattenhorn (2008) show that the cusp angle is consistent with the theoretical tidal stress field and linear elastic fracture mechanics models for mixed-mode I–II loading (Erdogan and Sih, 1963; Lawn, 1993; Pollard and Segall, 1987), revealing cycloid cusps to be analogous to tailcracks along terrestrial faults and joints.

On Europa, strike-slip faults exhibit two distinctive surface morphologies: discrete cracks with raised edifices (ridges), or tabular zones (bands) that formed through separation of the ice shell and infill by material from below (Kattenhorn, 2004). An examination of the intersection angles of tailcracks at the tips of these faults reveals that the band-like faults have lower intersection angles than ridge-like faults, suggesting that band-like faults dilated as they sheared, thus accounting for the band-like morphology, whereas ridge-like faults formed with the crack walls in frictional contact during shearing.

Considering the effects of a diurnally varying stress field acting on pre-existing fractures has also proven useful in explaining the relationship between fracture offsets (involving combinations of shearing, opening, and closing) and jet activity on Enceladus (Hurford et al., 2007; Nimmo et al., 2007; Smith-Konter and Pappalardo, 2008). The south-polar region of Enceladus is a tectonically active domain that exhibits a prominent fracture set (informally known as tiger stripes) surrounded by a region of inferred crustal convergence and folding (Porco et al., 2006; Fig. 15). The Cassini spacecraft has imaged water-ice jets emanating from these cracks on several occasions (Hansen et al., 2008), raising the question of how jet activity relates to the tectonics. By utilizing a Coulomb failure criterion, Smith-Konter and Pappalardo (2008) developed predictions of fault offsets, concluding that for sufficiently low

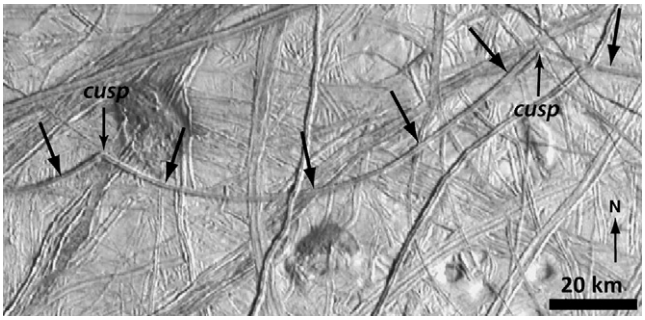

Fig. 14. Example of a curved, cuspate fracture on Europa called a cycloid. These curved cracks are inferred to grow during the diurnal tidal cycle in response to the rotating far-field stress direction. Consecutive cycloid segments grow during different Europan orbits and are joined at sharp cusps (from Galileo image mosaic 15ESREGMAP01).

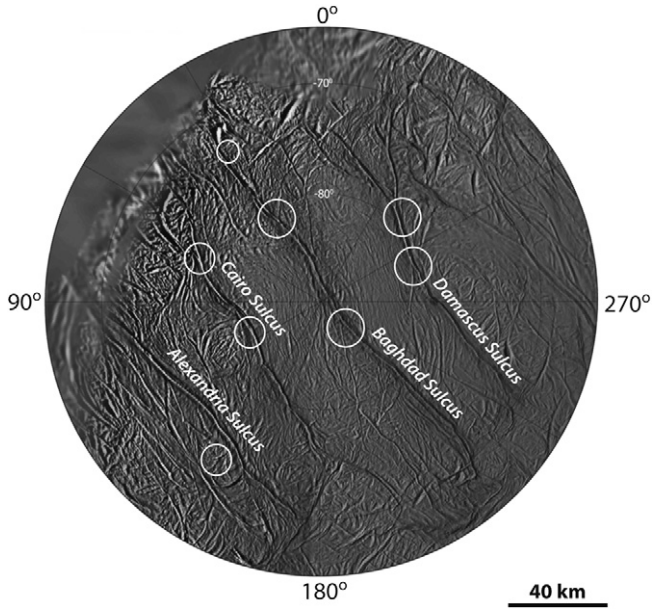

Fig. 15. The south-polar terrain on Enceladus (Cassini image SE_500K_90S_0_STEREO.IMG; Roatsch et al., 2008). The four most prominent fractures, informally named tiger stripes, are the apparent source of water-ice jets (white circles) that were imaged by the Cassini spacecraft.

friction coefficients ($\mu = 0.1–0.2$), the diurnal stress field could induce strike-slip faulting in particular locations that correlate with jet sources along the cracks (Fig. 15).

The theoretical magnitudes of a diurnally varying stress field are typically quite small (a few tenths of a megapascal) and may therefore be overprinted by larger magnitude stress sources that then control the structural evolution of the ice shell (e.g., Greenberg et al., 1998). Possible sources of these longer-term stresses include: (1) Nonsynchronous rotation: tidal torques on satellites in eccentric orbits may result in a slow nonsynchronous rotation of the body, resulting in locations on the surface moving longitudinally across the tidal bulges and inducing stresses in the ice shell (Greenberg and Weidenschilling, 1984; Helfenstein and Parmentier, 1985; Ojakangas and Stevenson, 1989a). (2) True polar wander: latitudinal migration of the ice shell in response to latitudinal variations in ice thickness will induce stresses in the shell (Ojakangas and Stevenson, 1989a, 1989b; Leith and McKinnon, 1996; Matsuyama and Nimmo, 2008). (3) Ice shell thickening: slow cooling of a liquid ocean within an icy satellite will result in a gradual shell thickening that will impart an isotropic component of stress on the extant stress field (Nimmo, 2004; Manga and Wang, 2007).

The implications of these long-term sources of stress have been considered for several icy satellites. Nonsynchronous rotation stresses are commonly invoked to explain the global distribution of fractures on Europa (Helfenstein and Parmentier, 1985; McEwen, 1986; Geissler et al., 1998; Greenberg et al., 1998; Figueredo and Greeley, 2000; Kattenhorn, 2002; Wahr et al., 2009). Matsuyama and Nimmo (2008) consider the implications of true polar wander on Europa and Enceladus and conclude that the orientations of extensional and contractional structures in different locations on the surface are consistent with a 90° reorientation of the surface. Ice shell thickening on Enceladus, and its implications for creating shell-penetrating cracks, has been examined by Manga and Wang (2007) and Rudolph and Manga (2008). A change in global shape, perhaps related to an increase in rotation rate (Collins and Schenk, 1994) or the circularization of an elliptical orbit (Prockter et al., 2005), has been suggested to be the cause of linear structures on Triton. Global expansion, perhaps related to internal differentiation, has been invoked to explain pervasive normal faulting on Ganymede (Collins et al., 1998).

On a more regional scale, analytical equations that describe flexure in an elastic plate (Watts, 2001; Turcotte and Schubert, 2002) have been used to explain the surface topographic profile shape and parallel tension fractures alongside surface loads on Europa (Nimmo et al., 2003; Billings and Kattenhorn, 2005; Hurford et al., 2005) (Fig. 16). Reasonable approximations of elastic properties of an ice shell thus allow estimates to be made of the elastic thickness beneath the surface load during flexure (e.g., 0.2–2 km on Europa; Billings and Kattenhorn, 2005).

4.2. Displacement-length scaling on Mars

Quantifying the relationship between maximum displacement and length (D_{max}/L) for faults and joints supports studies of deformation on planetary surfaces by providing insight into fracture interaction, population strain, and stratigraphic restriction (e.g., Schultz et al., 2006, 2008b, 2010). Measurements of the displacements and lengths of fractures on planetary surfaces with sufficient accuracy for detailed D_{max}/L scaling analyses had been available in

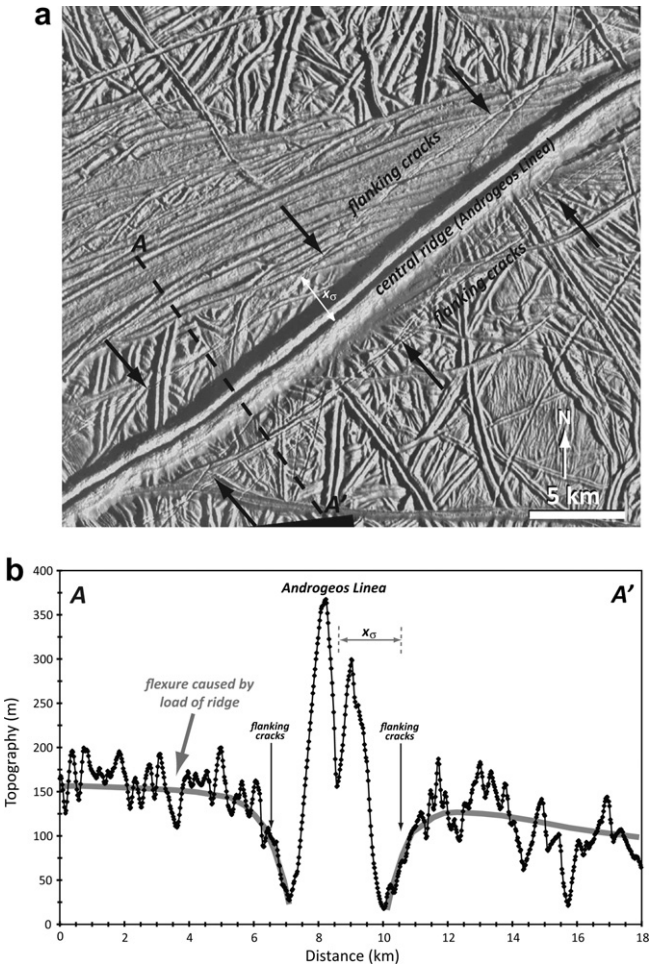

Fig. 16. (a) Example of a ridge on Europa, named Androgeos Linea, that is inferred to have caused the ice shell to flex downward under its weight (Galileo mosaic E6ESBRTPLN02). The flexure apparently resulted in flanking cracks at distance x_σ to either side of the ridge (black arrows). (b) Topographic profile across Androgeos Linea (location shown in (a) as dashed line) derived from photoclinometry and stereogrammetry. The inferred flexure shape is illustrated by the gray line. Topographic roughness is caused by the older ridges to either side of Androgeos Linea.

the literature only for faults that exceed ~10 km in length on the terrestrial planets (e.g., Schultz, 1997; Watters et al., 2000; Wilkins et al., 2002; Hauber and Kronberg, 2005).

Studies of planetary D_{max}/L scaling at length scales of less than 10 km are most promising on the surface of Mars, owing to the abundance of exposed and minimally cratered bedrock and the availability of sufficiently high resolution, orbiter-based imagery; these new results are now described. Early observations from MOC revealed the presence of many faults and joints at this scale, but sufficient resolution was not available to accurately measure fracture displacements.

Sub–meter resolution of fracture lengths and displacements on Mars has only recently become available from HiRISE. The planet's layered sedimentary deposits are found to exhibit clear examples of fractures that occur at length scales of 1 km or less (Okubo and McEwen, 2007; Nahm and Schultz, 2007; Okubo et al., 2008; 2009; Okubo, in press). A particularly well-exposed outcropping of sub-km-scale joints has been recently discovered in southwest Candor Chasma, within the layered sedimentary deposits at the bottom of the canyon (Fig. 17). DEMs derived from stereo HiRISE images indicate that these joints are sub-vertical, dipping at 82° ± 2° (Fig. 6). The highest resolution HiRISE observation of this area (PSP_001984_1735) has a ground-sampling dimension of 0.26 m per pixel. At this scale, the shape of objects that are ~1 m in diameter can be resolved. Based on these image data, we present here new measurements of the displacements and lengths for these joints.

Opening displacement and length are measured only along Martian joints that do not apparently terminate against another fracture, as resolved in the HiRISE data. Measurements of joints that intersect adjacent fractures are not reported here, as such measurements would largely contribute scatter to the D_{max}/L scaling results (e.g., Cartwright et al., 1995) and deserve a separate detailed treatment. Joint terminations are here considered to be located where the fracture can no longer be detected in the HiRISE data. An infilling of dark-toned sand (e.g., Okubo and McEwen, 2007) aids in highlighting the along-strike continuation of the joints down to the one pixel limit of detection. While the fracture must continue beyond this limit, the absolute termination cannot be pinpointed without 1-cm-scale, or finer, observations, which are not currently available for this study area.

Opening displacement along these joints is measured as the perpendicular distance between meter-scale tie points on opposing sides of the fracture (e.g., dovetailing asperities and bedrock layers; Fig. 17). Given that asperities on opposing fracture walls can be clearly tied together down to the limit of image detection, uncertainties in fracture aperture due to erosion of the fracture walls and obscuration by any mantling deposits is taken to be on the order of one pixel-width or less. Thus uncertainties associated with these measurements are within 1 pixel on each side of the joint, or conservatively 2 pixels (~0.52 m) for each measurement.

In this area, 32 joints exhibit displacements that can be measured in accordance with the estimated uncertainty and also do not appear to be connected to an adjacent fracture. Measurements between multiple tie-points along each fracture are used to establish the distribution of displacement, for apertures greater than 2 pixels (0.52 m). Inspection of the HiRISE imagery reveals a predominantly opening-mode sense of displacement between tie points on either side of the joints, with the displacement vector being approximately normal to the plane of the fracture. The resulting displacement profiles (e.g., Fig. 18) show that the maximum measured opening displacement occurs approximately at the center of the joint, indicating that mechanical interactions with adjacent fractures are minimal (e.g., Cartwright et al., 1995; Fossen and Hesthammer, 1997).

Measured Martian joint lengths are between 97.0 and 281.3 m, and maximum opening displacements are in the range of 0.58–5.33 m (Fig. 18). The mean D_{max}/L ratio for this set of joints is found to be 4.5×10^{-3} ($\pm 1.9 \times 10^{-3}$). While there is significant scatter in these values, linear regression analysis reveals a power-law scaling relationship between D_{max} and L, with $D_{max} = 0.061\ L^{0.532}$ ($R^2 = 0.40$). Similar sublinear power-law scaling relationships (dashed lines in Fig. 19) have been documented along terrestrial veins and dikes (Olson, 2003) and along deformation and compaction bands (Fossen and Hesthammer, 1997; Schultz et al., 2008b; Tembe et al., 2008; Schultz, 2009).

Igneous dikes are also being discovered in high-resolution images of the Coprates Chasma region of Valles Marineris. Study of these dikes is ongoing, and to date the opening displacements and lengths of only four dikes have been measured (Fig. 19). The mean D_{max}/L ratio for this small sample of dikes is found to be 4.0×10^{-3} ($\pm 3.0 \times 10^{-3}$), which is comparable to measurements of the larger set of joints in Candor Chasma.

The scaling relationships for D_{max} and L reported here are the first of their kind for joints and dikes on Mars. The joints and dikes measured here are of a comparable length (or slightly longer) than other opening-mode fractures (dikes) measured in the Ship Rock region of northwest New Mexico (Delaney and Pollard, 1981; Olson, 2003). Displacements along the Martian fractures however, are generally smaller than for Ship Rock dikes of comparable length, that is, the Martian fractures are under-displaced relative to terrestrial fractures of comparable length. The Martian fractures are likely to be somewhat more under-displaced than apparent on Fig. 19 since these lengths are only minimum values.

Under-displacement of fractures on planetary surfaces, relative to terrestrial counterparts, is common to fault data sets as

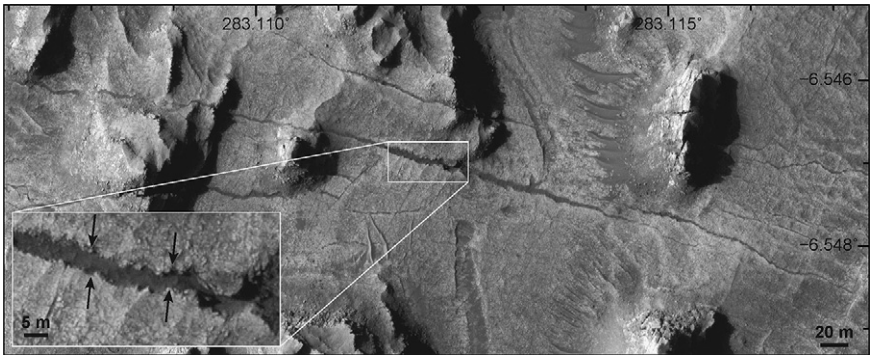

Fig. 17. Joints within the layered sedimentary deposits in west Candor Chasma, Mars. Maximum opening displacement is exhibited near the mid point of each joint. Inset shows examples of asperities along the joint walls that are used to measure the distribution of displacement. HiRISE image PSP_001918_1735, with illumination from the upper left. Inset is at full image resolution (26 cm/pixel).

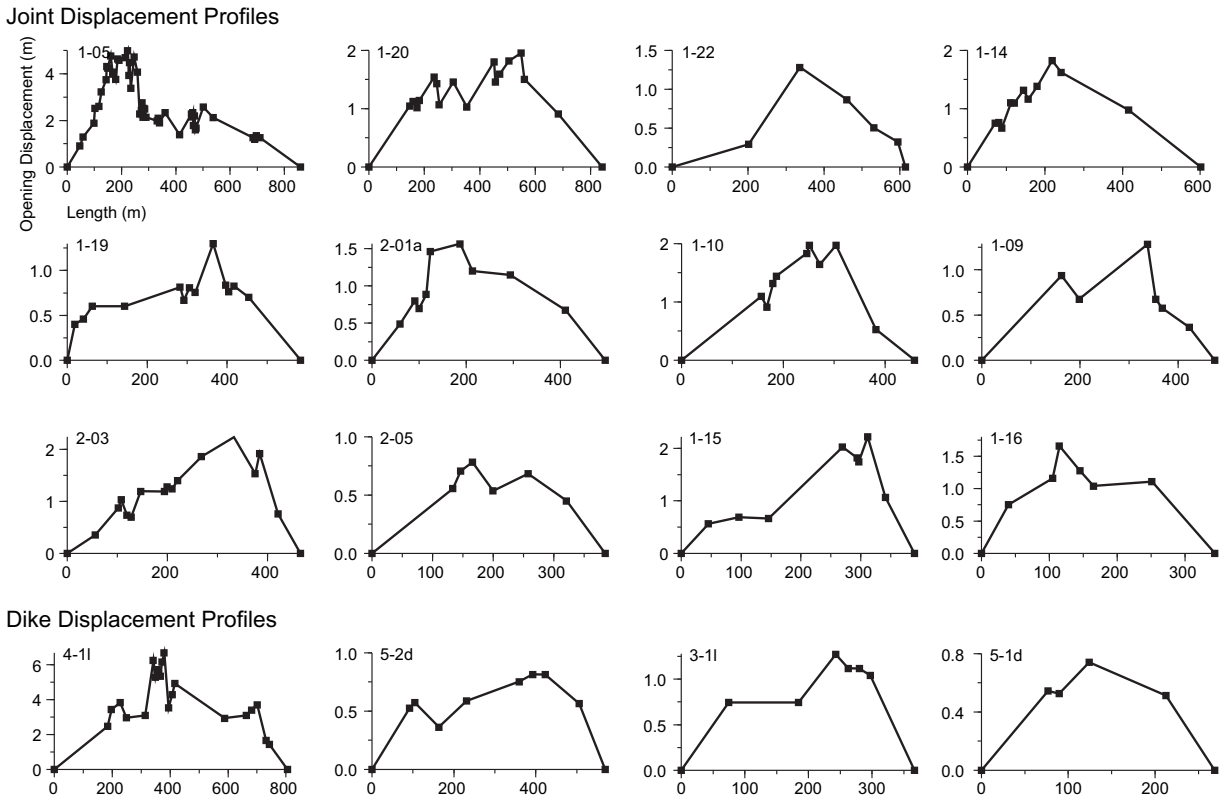

Fig. 18. Selected profiles of opening-mode displacement between tie-points along opposing walls of joints in west Candor Chasma and igneous dikes in Coprates Chasma, Mars. The *x*-axis (length) is the distance along the visible trace of the fracture.

well. Displacement-to-length ratios are typically 6.0×10^{-3} or 6.7×10^{-3} for faults on Mars (Watters et al., 1998; Wilkins et al., 2002) and 6.5×10^{-3} for faults on Mercury (Watters et al., 2000, 2002). On Earth, this ratio is typically between 2×10^{-2} and 5×10^{-2} over a range of tectonic settings and rock types (Cowie and Scholz, 1992; Clark and Cox, 1996; Schlische et al., 1996; Schultz and Fossen, 2002; Davis et al., 2005). Under–displacement of faults on Mercury and Mars can be attributed to these planets' smaller gravitational accelerations relative to Earth (Schultz et al., 2006). The ratio of a fault's displacement to its length is a function of the deformation modulus (the outcrop-scale equivalent of Young's modulus; Bieniawski, 1989) of the surrounding rock mass, the yield strength of the rock near the fault tip, and driving stress acting to displace the fault (Schultz et al., 2006). Deformation modulus, yield strength and driving stress are proportional to gravity and are smaller in magnitude on Mercury and Mars relative to Earth for a constant depth, groundwater condition and intact rock strength (Schultz et al., 2006). Thus the observed under-displacement is an expected characteristic for faults, and likely for opening-mode structures such as joints and dikes as well, on all planets and satellites because they have less mass than the Earth.

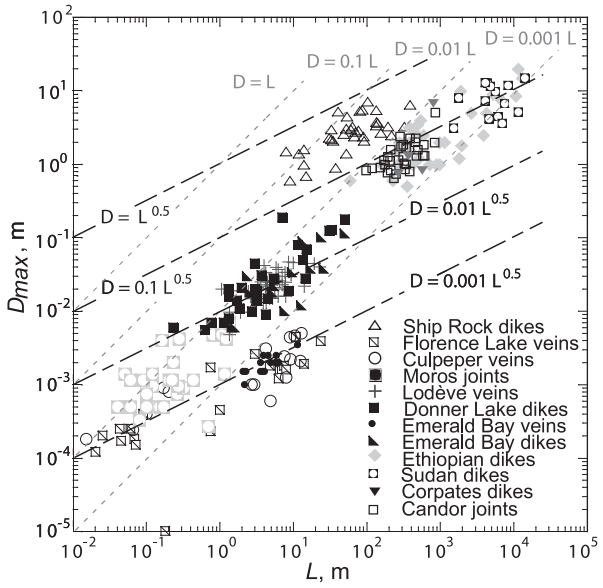

Fig. 19. Displacement-length (D_{max}/L) scaling of opening-mode fractures from Earth (after Olson, 2003; Schultz et al., 2008b; Klimczak et al., in press) and Mars (Coprates dikes and Candor joints, this paper). Lines of constant slope are shown: $n = 1$ is dotted (appropriate to faults with linear D_{max}/L scaling), with $D_{max}/L = \gamma$; $n = 0.5$ is dashed.

The abundance of opening displacement and length measurements for the joints in Candor Chasma enable calculations of apparent fracture toughness (K_{Ic}) for the layered sedimentary deposits. D_{max} scales with L as

$$D_{max} = CL^n \quad (2)$$

with the exponent n equal to 0.5 for fractures propagating under constant stress intensity factor conditions, and $n = 1.0$ for fracture propagation under constant driving stress (Olson, 2003). The observed power-law scaling of D_{max} and L for the Candor joints ($n = 0.532$) indicates within the uncertainty of this technique that these fractures, as with other mode-I fractures (Schultz et al.,

2008b), propagated under constant stress intensity factor conditions, rather than in response to a constant driving stress.

Under constant stress intensity factor conditions,

$$C = \frac{K_{Ic}(1-\nu^2)}{E^*\sqrt{\pi/8}} \quad (3)$$

(Olson, 2003). Thus values of K_{Ic} can be determined for the Candor joints with knowledge of the deformation modulus (E^*) and Poisson's ratio (ν) of the host rock. Values of E^* are estimated by assuming a rock mass rating (RMR) of 30–55, as previously determined for the layered sedimentary deposits (Schultz, 2002), and using empirically-derived relationships between RMR and E^* (e.g., Bieniawski, 1989; Schultz, 1996). This yields values for E^* between 3.2 and 10 GPa. Further, a range of values for ν between 0.2 and 0.3, the typical range for rocks on Earth, is adopted. Given that the best-fit value for n approximates the theoretical value of 0.5, the value of C in Eq. (3) is taken to be 0.061, as calculated directly from the linear regression analysis for the entire population of Candor joints. Solving Eq. (3) for K_{Ic}, over these ranges of E^*, ν, and C, yields values for K_{Ic} of 127–420 MPa $m^{0.5}$.

Measurements of the Ship Rock dike segments show D_{max} scales with L as $D_{max} = 0.43\,L^{0.40}$ ($R^2 = 0.55$) (Olson, 2003). These dikes show a similar affinity toward propagation under constant stress intensity factor conditions ($n \approx 0.5$). Setting $n = 0.5$ for the Ship Rock data gives $C = 0.27$ and yields corresponding values for K_{Ic} of 40–4000 MPa $m^{0.5}$ (Olson, 2003).

The values of K_{Ic} for the Candor joints (and Ship Rock dikes) are much larger than values calculated in the same way for m- to cm-scale veins on Earth, which fall within the range of 8–25 MPa $m^{0.5}$ (Olson, 2003). In comparison, values of K_{Ic} extracted from laboratory testing of cm-scale samples typically fall within the 1–10 MPa $m^{0.5}$ range (Atkinson and Meredith, 1987). As discussed by Olson (2003) and others, there are several possible causes for the larger than expected values of K_{Ic} for the Ship Rock dikes. These include the temperature dependent behavior of K_{Ic} (DeGraff and Aydin, 1993; Balme et al., 2004; Schultz et al., 2008a), mechanical interaction between adjacent segments (Delaney and Pollard, 1981), and the effects of process zones surrounding fractures (Pollard, 1987). The Candor joints lack evidence of thermal alteration, thus temperature effects appear unlikely, but are not completely ruled out. Some mechanical interaction between these joints may have occurred. Displacement is not entirely symmetric about the center of the joints, as is predicted for completely isolated fractures (e.g., Pollard and Segall, 1987). Elevated values of fracture toughness can arise for opening-mode fractures that propagate within layers that are sufficiently thin relative to fracture length (Schultz et al., 2008a). Process zones along the Candor joints are also a possible source of the larger values for K_{Ic}. Process zones are observed along terrestrial fractures of similar length scale (Delaney et al., 1986), and the discontinuities that comprise these process zones in clastic rocks (deformation bands; Fossen et al., 2007) have been observed around faults in other layered sedimentary rocks on Mars (Okubo et al., 2009).

5. Discussion and conclusions

Working in planetary structural geology offers both challenges and opportunities relative to terrestrial studies. First, faults, folds, and other structures can be more clearly expressed on other planets and satellites given the favorable combination of low erosion and deposition rates (due to thin or non-existent atmospheres), excellent exposure (due in part to lack of vegetation), and in some cases (but not all), a simpler record of deformation. In such cases, the astute structural geologist will recognize commonalities between terrestrial and planetary structures, such as relay ramps and displacement minima along normal faults, characteristic topographic signatures, or secondary structures indicating strike-slip offset, that can be used to interpret planetary faults with the same degree of confidence as terrestrial ones. Second, although the datasets and exposures are excellent in many cases down to the outcrop scale, the lack of ability to physically visit a site generally requires that the planetary structural geologist be more systematic, more rigorous, and perhaps less prone to speculation than his or her Earth-based counterpart in order to produce believable and high-quality science.

The suite of results presented in this paper illustrates the high quality of observational data and level of interpretation that are now available to structural geologists working on the solid-surface planets and satellites. While a knowledge of terrestrial structures and their causative deformation processes and stress states is an essential tool for identifying and working with planetary structures, many unique structural and tectonic problems exist on the planets and satellites whose analysis can enrich our understanding of tectonic processes in general and those on the Earth in particular. Conversely, continuing analysis of planetary structures from bodies located throughout the solar system substantiate the view that terrestrial-style plate tectonics, characterized by horizontally mobile lithospheric plates with concomitant seafloor spreading and plate subduction that is maintained over geologic timescales, is unique to the Earth. Planetary structural geology thus presents an opportunity to test and expand an Earth-based understanding of fundamental tectonic processes across a wide spectrum of planetary geodynamics.

Acknowledgments

Thorough and helpful reviews by David Peacock and Robert Pappalardo helped streamline and sharpen the final paper. This work was supported by grants from NASA's Planetary Geology and Geophysics Program and the Mars Data Analysis Program to RAS. SAK acknowledges grants from NASA's Planetary Geology and Geophysics (NNX06AC12G and NNX08AK71G) and Outer Planets Research (NNX08AQ94G) Programs. CHO acknowledges support through Mars Data Analysis Program grant NNX06AE01G. TRW acknowledges support from NASA's Planetary Geology and Geophysics Program grant NNX08AM19G and from NASA grant NNX07AR60G. EH was partly supported by the Helmoltz Association through the research alliance "Planetary Evolution and Life". Thanks to Jason Barnes, Terry Hurford, Christina Coulter, Paul Schenk, and Christian Klimczak for providing their expertise on various facets of this work. We thank Marie Dowling of the National Space Science Data Center for providing the Apollo 10 image of Rima Ariadaeus.

References

Ackermann, R.V., Schlische, R.W., Withjack, M.O., 2001. The geometric and statistical evolution of normal fault systems: an experimental study of the effects of mechanical layer thickness on scaling laws. Journal of Structural Geology 23, 1803–1819.

Anderson, E.M., 1951. The Dynamics of Faulting and Dyke Formation, with Applications to Britain. Oliver & Boyd, Edinburgh, pp. 206.

Andrews-Hanna, J.C., Phillips, R.J., Zuber, M.T., 2007. Meridiani Planum and the global hydrology of Mars. Nature 446, 163–166.

Andrews-Hanna, J.C., Zuber, M.T., Hauk II, S.A., 2008. Strike-slip faults on Mars: observations and implications for global tectonics and geodynamics. Journal of Geophysical Research 113, E08002. doi:10.1029/2007JE002980.

Arvidson, R.E., Goettel, K.A., Hohenberg, C.M., 1980. A post-Viking view of Martian geologic evolution. Reviews of Geophysics and Space Physics 18, 565–603.

Atkinson, B.K., Meredith, P.G., 1987. Experimental Fracture Mechanics Data for Rocks and Minerals. In: Atkinson, B.K. (Ed.), Fracture Mechanics of Rock. Academic, London, pp. 477–525.

Aydin, A., 2006. Failure modes of the lineaments on Jupiter's moon, Europa: implications for the origin of its icy crust. Journal of Structural Geology 28, 2222–2236.
Aydin, A., Borja, R.I., Eichhubl, P., 2006. Geological and mathematical framework for failure modes in granular rock. Journal of Structural Geology 28, 83–98.
Balme, M.R., Rocchi, V., Jones, C., Sammonds, P.R., Meredith, P.G., Boon, S., 2004. Fracture toughness measurements on igneous rocks using a high-pressure, high-temperature rock fracture mechanics cell. Journal of Volcanology and Geothermal Research 132, 159–172.
Banerdt, W.B., Golombek, M.P., Tanaka, K.L., 1992. Stress and tectonics on Mars. In: Kieffer, H.H., Jakosky, B.M., Snyder, C.W., Matthews, M.S. (Eds.), Mars. Univ. Arizona Press, Tucson, pp. 249–297.
Beatty, J.K., Peterson, C.C., Chaikin, A., 1999. The New Solar System, fourth ed. Cambridge University Press.
Barnett, J.A.M., Mortimer, J., Rippon, J.H., Walsh, J.J., Watterson, J., 1987. Displacement geometry in the volume containing a single normal fault. American Association of Petroleum Geologists Bulletin 71, 925–937.
Billings, S.E., Kattenhorn, S.A., 2005. The great thickness debate: ice shell thickness models for Europa and comparisons with estimates based on flexure at ridges. Icarus 177, 397–412.
Binder, A.B., Gunga, H.-C., 1985. Young thrust-fault scarps in the highlands: evidence for an initially totally molten moon. Icarus 63, 421–441.
Byerlee, J., 1978. Friction of rocks. Pure and Applied Geophysics 116, 615–626. doi:10.1007/BF00876528.
Bieniawski, Z.T., 1989. Engineering Rock Mass Classifications: a Complete Manual for Engineers and Geologists in Mining, Civil, and Petroleum Engineering. Wiley & Sons, New York.
Bryan, W.B., 1973. Wrinkle-ridges as deformed surface crust on ponded mare lava. Geochimica et Cosmochimica Acta 1 (Suppl.), 93–106.
Cailleau, B., Walter, T.R., Janle, P., Hauber, E., 2003. Modeling volcanic deformation in a regional stress field: implications for the formation of graben structures on Alba Patera, Mars. Journal of Geophysical Research 108, 5141. doi:10.1029/2003JE002135.
Carr, M.H., 1980. The morphology of the Martian surface. Space Science Reviews 25, 231–284.
Cartwright, J.A., Trudgill, B.D., Mansfield, C.S., 1995. Fault growth by segment linkage: an explanation for scatter in maximum displacement and trace length data from the Canyonlands Grabens of SE Utah. Journal of Structural Geology 17, 1319–1326.
Chin, G., Brylow, S., Foote, M., Garvin, J., Kasper, J., Keller, J., Litvak, M., Mitrofanov, I., Paige, D., Raney, K., Robinson, M., Sanin, A., Smith, D., Spence, H., Spudis, P., Stern, S., Zuber, M., 2007. Lunar Reconnaissance Orbiter overview: the instrument suite and mission. Space Science Reviews 219, 391–419. doi:10.1007/s11214-007-9153-y.
Christensen, P.R., Jakosky, B.M., Kieffer, H.H., Malin, M.C., McSween, H.Y., Nealson, K., Mehall, G.L., Silverman, S.H., Ferry, S., Caplinger, M., Ravine, M., 2004. The thermal emission imaging system (THEMIS) for the Mars 2001 Odyssey mission. Space Science Reviews 110, 85–130. doi:10.1023/B:SPAC.0000021008.16305.94.
Clark, R.M., Cox, S.J.D., 1996. A modern regression approach to determining fault displacement-length relationships. Journal of Structural Geology 18, 147–152.
Collins, G.C., Head, J.W., Pappalardo, R.T., 1998. Formation of Ganymede grooved terrain by sequential extensional episodes: implications of Galileo observations for regional stratigraphy. Icarus 135, 345–359.
Collins, G., Schenk, P., 1994. Triton's lineaments: complex morphology and stress patterns. Proceedings of Lunar Science Conference 25, 277–278.
Collins, G.C., McKinnon, W.B., Moore, J.M., Nimmo, F., Pappalardo, R.T., Prockter, L.M., Schenk, P.M., 2010. Tectonics of the outer planet satellites. In: Watters, T.R., Schultz, R.A. (Eds.), Planetary Tectonics. Cambridge University Press, pp. 264–350.
Cowie, P.A., Scholz, C.H., 1992. Displacement-length scaling relationships for faults: data synthesis and discussion. Journal of Structural Geology 14, 1149–1156.
Cowie, P.A., Roberts, G.P., Mortimer, E., 2007. Strain localization within fault arrays over timescales of 10^0–10^7 years. In: Handy, M.R., Hirth, G., Hovius, N. (Eds.), Tectonic Faults: Agents of Change on a Dynamic Earth. MIT Press, Cambridge, pp. 47–77. Dahlem Workshop Report 95.
Crider, J.G., Pollard, D.D., 1998. Fault linkage: three-dimensional mechanical interaction between echelon normal faults. Journal of Geophysical Research 103, 24373–24391.
Cunningham, W.D., Mann, P., 2007. Tectonics of restraining and releasing bends. In: Cunningham, W.D., Mann, P. (Eds.), Tectonics of Strike-Slip Restraining and Releasing Bends. Geological Society, London, Special Publications, vol. 290, pp. 1–12.
Davis, K., Burbank, D.W., Fisher, D., Wallace, S., Nobes, D., 2005. Thrust-fault growth and segment linkage in the active Ostler fault zone, New Zealand. Journal of Structural Geology 27, 1528–1546. doi:10.1016/j.jsg.2005.04.011.
Davison, I., 1994. Linked fault systems; extensional, strike-slip and contractional. In: Hancock, P.L. (Ed.), Continental Deformation. Pergamon, New York, pp. 121–142.
DeGraff, J.M., Aydin, A., 1993. Effect of thermal regime on growth increment and spacing of contraction joints in basaltic lava. Journal of Geophysical Research 98, 6411–6430.
DeRemer, L.C., Pappalardo, R.T., 2003. Manifestations of strike-slip faulting on Ganymede. Proc. Lunar Sci. Conf. XXXIV, abstract #2033.
Delamere, W.A., Tornabene, L.L., McEwen, A.S., Becker, K., Bergstrom, J.W., Bridges, N.T., Eliason, E.M., Gallagher, D., Herkenhoff, K.E., Keszthelyi, L., Mattson, S., McArthur, G.K., Mellon, M.T., Milazzo, M., Russell, P.S., Thomas, N., 2010. Color imaging of Mars by the High Resolution Imaging Science Experiment (HiRISE). Icarus 205, 38–52. doi:10.1016/j.icarus.2009.03.012.
Delaney, P.T., Pollard, D.D., 1981. Deformation of host rocks and flow of magma during growth of minette dikes and breccia-bearing intrusions near Ship Rock, New Mexico. U.S. Geological Survey Professional Paper 1202.
Delaney, P.T., Pollard, D.D., Ziony, J.I., McKee, E.H., 1986. Field relations between dikes and joints: emplacement processes and paleostress analysis. Journal of Geophysical Research 91, 4920–4938.
Dzurisin, D., 1978. The tectonic and volcanic history of Mercury as inferred from studies of scarps, ridges, troughs, and other lineaments. Journal of Geophysical Research 83, 4883–4906.
Earth Impact Database, 2007. http://www.unb.ca/passc/ImpactDatabase.
Erdogan, F., Sih, G.C., 1963. On the crack extension in plates under plane loading and transverse shear. Journal of Basic Engineering 85, 519–527.
Figueredo, P.H., Greeley, R., 2000. Geologic mapping of the northern leading hemisphere of Europa from Galileo solid-state imaging data. Journal of Geophysical Research 105, 22629–22646.
Figueredo, P.H., Greeley, R., 2004. Resurfacing history of Europa from pole-to-pole geological mapping. Icarus 167, 287–312.
Fossen, H., Hesthammer, J., 1997. Geometric analysis and scaling relations of deformation bands in porous sandstone. Journal of Structural Geology 19, 1479–1493.
Fossen, H., Schultz, R.A., Shipton, Z.K., Mair, K., 2007. Deformation bands in sandstone: a review. Journal of the Geological Society of London 164, 755–769.
Fueten, F., Stesky, R.M., MacKinnon, P., 2005. Structural attitudes of large scale layering in Valles Marineris, Mars, calculated from Mars Orbiter Laser Altimeter data and Mars Orbiter Camera imagery. Icarus 175, 68–77. doi:10.1016/j.icarus.2004.11.010.
Fueten, F., Stesky, R.M., MacKinnon, P., Hauber, E., Gwinner, K., Scholten, F., Zegers, T., Neukum, G., 2006. A structural study of an interior layered deposit in southwestern Candor Chasma, Valles Marineris, Mars, using High Resolution Stereo Camera data from Mars Express. Geophysical Research Letters 33, L07202. doi:10.1029/2005GL025035.
Fueten, F., Stesky, R.M., MacKinnon, P., Hauber, E., Zegers, T., Gwinner, K., Scholten, F., Neukum, G., 2008. Stratigraphy and structure of interior layered deposits in west Candor Chasma, Mars, from High Resolution Stereo Camera (HRSC) stereo imagery and derived elevations. Journal of Geophysical Research 118, E10008,. doi:10.1029/2007JE003053.
Geissler, P.E., Greenberg, R., Hoppa, G., Helfenstein, P., McEwen, A., Pappalardo, R., Tufts, R., Ockert-Bell, M., Sullivan, R., Greeley, R., Belton, M.J.S., Denk, T., Clark, B.E., Burns, J., Ververka, J., 1998. Evidence for non-synchronous rotation of Europa. Nature 391, 368–370.
Giese, B., Wagner, R., Neukum, G., Helfenstein, P., Thomas, P.C., 2006. Tethys: lithospheric thickness and heat flux from flexurally supported topography at Ithaca Chasma. Geophysical Research Letters 34, L21203,. doi:10.1029/2007GL031467.
Giese, B., Wagner, R., Hussm.ann, H., Neukum, G., Perry, J., Helfenstein, P., Thomas, P.C., 2008. Enceladus: an estimate of heat flux and lithospheric thickness from flexurally supported topography. Geophysical Research Letters 35, L24204. doi:10.1029/2008GL036149.
Goff-Pochat, N., Collins, G.C., 2009. Strain measurement across fault scarps on Dione. Lunar and Planetary Science Conference XL, abstract # 2111.
Golombek, M.P., Phillips, R.J., 2010. Mars tectonics. In: Watters, T.R., Schultz, R.A. (Eds.), Planetary Tectonics. Cambridge University Press, pp. 183–232.
Greenberg, R., Geissler, P., Hoppa, G., Tufts, B.R., Durda, D.D., Pappalardo, R., Head, J.W., Greeley, R., Sullivan, R., Carr, M.H., 1998. Tectonic processes on Europa: tidal stresses, mechanical response, and visible features. Icarus 135, 64–78.
Greenberg, R., Hoppa, G.V., Bart, G., Hurford, T., 2003. Tidal stress patterns on Europa's crust. Celestial Mechanics and Dynamical Astronomy 87, 171–188.
Greenberg, R., Weidenschilling, S.J., 1984. How fast do Galilean satellites spin? Icarus 58, 186–196.
Groenleer, J.M., Kattenhorn, S.A., 2008. Cycloid crack sequences on Europa: relationship to stress history and constraints on growth mechanics based on cusp angles. Icarus 193, 158–181.
Grott, M., Hauber, E., Werner, S.C., Kronberg, P., 2005. High heat flux on ancient Mars: evidence from rift flank uplift at Coracis Fossae. Geophysical Research Letters 32, L21201. doi:10.1029/2005GL023894.
Grotzinger, J.P., et al., 2005. Stratigraphy and sedimentology of a dry to wet eolian depositional system, Burns Formation, Meridiani Planum, Mars. Earth and Planetary Science Letters 240, 11–72.
Gwinner, K., Scholten, F., Spiegel, M., Schmidt, R., Giese, B., Oberst, J., Jaumann, R., Neukum, G., the HRSC Co-Investigator Team, 2005. Hochauflösende Digitale Geländemodelle auf der Grundlage von Mars Express HRSC-Daten. Photogrammetrie, Fernerkundung, Geoinformation 5, 387–394.
Gwinner, K., Scholten, F., Spiegel, M., Schmidt, R., Giese, B., Oberst, J., Heipke, C., Jaumann, R., Neukum, G., 2009. Derivation and validation of high-resolution digital elevation models from Mars Express HRSC data. Photogrammetric Engineering and Remote Sensing 75, 1127–1142.
Gwinner, K., Scholten, F., Preusker, F. Elgner, S., Roatsch, T., Spiegel, M., Schmidt, R., Oberst, J., Jaumann, R., Heipke, C. Topography of Mars from global mapping by HRSC high-resolution digital elevation models and orthoimages: characteristics

and performance. Earth and Planetary Science Letters, in press, doi:10.1016/j.epsl.2009.11.007.
Hansen, C.J., Esposito, L.W., Stewart, A.I.F., Meinke, B., Wallis, B., Colwell, J.E., Hendrix, A.R., Larsen, K., Pryor, W., Tian, F., 2008. Water vapour jets inside the plume of gas leaving Enceladus. Nature 456, 477–479.
Harrison, K.P., Grimm, R.E., 2009. Regionally compartmented groundwater flow on Mars. Journal of Geophysical Research 114, E04004. doi:10.1029/2008JE003300.
Hauber, E., Kronberg, P., 2001. Tempe Fossae, Mars: a planetary analog to a terrestrial continental rift? Journal of Geophysical Research 106, 20587–20602.
Hauber, E., Kronberg, P., 2005. The large Thaumasia graben on Mars: is it a rift? Journal of Geophysical Research 110, E07003. doi:10.1029/2005JE002407.
Hauber, E., Grott, M., Kronberg, P. Martian rifts: structural geology and geophysics. Earth and Planetary Science Letters, in press, doi:10.1016/j.epsl.2009.11.005.
Hauber, E., Charalambakis, E., Gwinner, K., Knapmeyer, M., Grott, M., 2007. Displacement-length relationships of normal faults on Mars: new observations with MOLA and HRSC (abstract). 7th International Conference on Mars, Lunar and Planetary Institute Contribution 1353, abstract 3110.
Hauck, S.A., Dombard, A.J., Phillips, R.J., Solomon, S.C., 2004. Internal and tectonic evolution of Mercury. Earth and Planetary Science Letters 222, 713–728.
Helfenstein, P., Parmentier, E.M., 1985. Patterns of fracture and tidal stresses on Europa. Icarus 61, 175–184.
Hoek, E., Brown, E.T., 1997. Practical estimates of rock mass strength. International Journal of Rock Mechanics and Mining Science & Geomechanics Abstracts 34, 1165–1186. doi:10.1016/S0148-9062(97)00305-7.
Hoppa, G., Tufts, B.R., Greenberg, R., Geissler, P., 1999a. Strike-slip faults on Europa: global shear patterns driven by tidal stress. Icarus 141, 287–298.
Hoppa, G.V., Tufts, B.R., Greenberg, R., Geissler, P.E., 1999b. Formation of cycloidal features on Europa. Science 285, 1899–1902.
Huntoon, P.W., 2000. Upheaval Dome, Canyonlands, Utah: strain indicators that reveal an impact origin. In: Sprinkel, D.A., Chidsey Jr., T.C., Anderson, B.P. (Eds.), Geology of Utah's Parks and Monuments. Utah Geological Association Publication 28.
Hurford, T.A., Beyer, R.A., Schmidt, B., Preblich, B., Sarid, A.R., Greenberg, R., 2005. Flexure of Europa's lithosphere due to ridge-loading. Icarus 177, 380–396.
Hurford, T.A., Helfenstein, P., Hoppa, G.V., Greenberg, R., Bills, B.G., 2007. Eruptions arising from tidally controlled periodic openings of rifts on Enceladus. Nature 447, 292–294.
Jaeger, J.C., Cook, N.G.W., 1979. Fundamentals of Rock Mechanics, third ed. Chapman and Hall, New York.
Jaumann, R., Neukum, G., Behnke, T., Duxbury, T.C., Eichentopf, K., Flohrer, J., van Gasselt, S., Giese, B., Gwinner, K., Hauber, E., Hoffmann, H., Hoffmeister, A., Köhler, U., Matz, K.-D., McCord, T.B., Mertens, V., Oberst, J., Pischel, R., Reiss, D., Ress, E., Roatsch, T., Saiger, P., Scholten, F., Schwarz, G., Stephan, K., Wählisch, M., the HRSC Co-Investigator Team, 2007. The High-Resolution Stereo Camera (HRSC) experiment on Mars Express: instrument aspects and experiment conduct from interplanetary cruise through the nominal mission. Planetary and Space Science 55, 928–952.
Kargel, J.S., Pozio, S., 1996. The volcanic and tectonic history of Enceladus. Icarus 119, 385–404.
Kattenhorn, S.A., 2002. Nonsynchronous rotation evidence and fracture history in the bright plains region, Europa. Icarus 157, 490–506.
Kattenhorn, S.A., 2004. Strike-slip fault evolution on Europa: evidence from tail-crack geometries. Icarus 172, 582–602.
Kattenhorn, S.A., Marshall, S.T., 2006. Fault-induced perturbed stress fields and associated tensile and compressive deformation at fault tips in the ice shell of Europa: implications for fault mechanics. Journal of Structural Geology 28, 2204–2221.
Kattenhorn, S.A., Hurford, T.A., 2009. Tectonics of Europa. In: Pappalardo, R.T., McKinnon, W.B., Khurana, K. (Eds.), Europa. University of Arizona Press, pp. 199–236.
Kenkmann, T., 2002. Folding within seconds. Geology 30, 231–234.
Kenkmann, T., Jahn, A., Scherler, D., Ivanov, B.A., 2005. Structure and formation of a central uplift: A case study at Upheaval Dome impact crater, Utah. In: Kenkmann, T., Horz, F., Deutsch, A., (Eds.), Large Meteorite Impacts III, Geological Society of America Special Paper 384, p. 85–115.
Kirk, R.L., Howington-Kraus, E., Rosiek, M., Anderson, J.A., Archinal, B., Becker, K.J., Cook, D.A., Galuszka, D., Geissler, P.E., Hare, T.M., Holmberg, I.M., Keszthelyi, L., Redding, B., Delamere, A., Gallagher, D., Chapel, J.D., Eliason, E.M., King, R.A., McEwen, A.S., 2008. Ultra-high-resolution topographic mapping of Mars with MRO HiRISE stereo images: meter-scale slopes of candidate Phoenix landing sites. Journal of Geophysical Research 113, E00A24. doi:10.1029/2007JE003000.
Klimczak, C., Schultz, R.A., Parashar, R., Reeves, D.M. Cubic law with aperture-length correlation: implications for network scale fluid flow. Hydrogeology Journal, in press.
Knapmeyer, M., Oberst, J., Hauber, E., Wählisch, M., Deuchler, C., Wagner, R., 2006. Working models for spatial distribution and level of Mars' seismicity. Journal of Geophysical Research 111, E11006. doi:10.1029/2006JE002708.
Kriens, B.J., Shoemaker, E.M., Herkenhoff, K.E., 1999. Geology of the Upheaval Dome impact structure, southeast Utah. Journal of Geophysical Research 104, 18867–18887.
Kronberg, P., Hauber, E., Grott, M., Werner, S.C., Schäfer, T., Gwinner, K., Giese, B., Masson, P., Neukum, G., 2007. Acheron Fossae, Mars: tectonic rifting, volcanism, and implications for lithospheric thickness. Journal of Geophysical Research 112, E04005. doi:10.1029/2006JE002780.
Laney, R.T., Van Schmus, W.R., 1978. A structural study of the Kentland, Indiana, impact site. Proceedings of Lunar and Planetary Science Conference 9th, 2609–2632.
Lawn, B., 1993. Fracture of Brittle Solids. Cambridge University Press, Cambridge, pp. 378.
Leith, A.C., McKinnon, W.B., 1996. Is there evidence for polar wander on Europa? Icarus 120, 387–398.
Lucchitta, B.K., Bertolini, L.M., 1989. Interior structures of Valles Marineris. Proceedings of Lunar and Planetary Science Conference 20, 590–591.
Lucchitta, B.K., Isbell, N., Howington-Kraus, A., 1994. Topography of Valles Marineris: implications for erosional and structural history. Journal of Geophysical Research 99, 3783–3798. doi:10.1029/93JE03095.
Lucchitta, B.K., McEwen, A.S., Clow, G.D., Geissler, P.E., Singer, R.B., Schultz, R.A., Squyres, S.W., 1992. The canyon system on Mars. In: Kieffer, H.H., Jakosky, B.M., Snyder, C.W., Matthews, M.S. (Eds.), Mars. Univ. Arizona Press, Tucson, pp. 453–492.
Malin, M.C., Edgett, K.S., 2001. Mars Global Surveyor Mars Orbiter Camera: interplanetary cruise through primary mission. Journal of Geophysical Research 106, 23429–23570. doi:10.1029/2000JE001455.
Malin, M.C., Bell, J.F., Cantor, B.A., Caplinger, M.A., Calvin, W.M., Clancy, R.T., Edgett, K.S., Edwards, L., Haberle, R.M., James, P.B., Lee, S.W., Ravine, M.A., Thomas, P.C., Wolff, M.J., 2007. Context camera investigation on board the Mars Reconnaissance Orbiter. Journal of Geophysical Research 112, E05S04. doi:10.1029/2006JE002808.
Manga, M., Wang, C.-Y., 2007. Pressurized oceans and the eruption of liquid water on Europa and Enceladus. Geophysical Research Letters 34, L07202. doi:10.1029/2007GL029297.
Manighetti, I., Campillo, M., Sammis, C., Mai, P.M., King, G., 2005. Evidence for self-similar, triangular slip distributions on earthquakes: implications for earthquake and fault mechanics. Journal of Geophysical Research 110, B05302. doi:10.1029/2004JB003174.
Mansfield, C., Cartwright, J., 2001. Fault growth by linkage: observations and implications from analogue models. Journal of Structural Geology 23, 745–763.
Margot, J.L., Peale, S.J., Jurgens, R.F., Slade, M.A., Holin, I.V., 2007. Large longitude libration of Mercury reveals a molten core. Science 316, 710–714.
Marshall, S.T., Kattenhorn, S.A., 2005. A revised model for cycloid growth mechanics on Europa: evidence from surface morphologies and geometries. Icarus 177, 341–366.
Masursky, H., Colton, G.W., El-Baz, F. (Eds.), 1978. Apollo Over the Moon: A View from Orbit. NASA Special Paper SP–362, 255 pp., Washington, D.C.
Matsuyama, I., Nimmo, F., 2008. Tectonic patterns on reoriented and despun planetary bodies. Icarus 195, 459–473.
Maxwell, T.A., El-Baz, F., Ward, S.W., 1975. Distribution, morphology, and origin of ridges and arches in Mare Serenitatis. Geological Society of America Bulletin 86, 1273–1278.
McEwen, A.S., 1986. Tidal reorientation and the fracturing of Jupiter's moon Europa. Nature 321, 49–51.
McEwen, A.S., Eliason, E.M., Bergstrom, J.W., Bridges, N.T., Hansen, C.J., Delamere, W.A., Grant, J.A., Gulick, V.C., Herkenhoff, K.E., Keszthelyi, L., Kirk, R.L., Mellon, M.T., Squyres, S.W., Thomas, N., Weitz, C.M., 2007. Mars Reconnaissance Orbiter's High Resolution Imaging Science Experiment (HiRISE). Journal of Geophysical Research 112, E05S02. doi:10.1029/2005JE002605.
McGill, G.E., 1971. Attitude of fractures bounding straight and arcuate lunar rilles. Icarus 14, 53–58.
McGill, G.E., Stofan, E.R., Smrekar, S.E., 2010. Venus Tectonics. In: Watters, T.R., Schultz, R.A. (Eds.), Planetary Tectonics. Cambridge University Press, pp. 81–120.
Mège, D., Masson, P.L., 1996. A plume tectonics model for the Tharsis province, Mars. Planetary and Space Science 44, 1499–1546.
Melosh, H.J., 1978. The tectonics of mascon loading. Proceedings of Lunar Science Conference 9, 3513–3525.
Melosh, H.J., McKinnon, W.B., 1988. The tectonics of Mercury. In: Vilas, F., Chapman, C.R., Matthews, M.S. (Eds.), Mercury. University of Arizona Press, Tucson.
Moore, J.M., Schultz, R.A., 1999. Processes of faulting in jointed rocks of Canyonlands National Park, Utah. Geological Society of America Bulletin 111, 808–822.
Morley, C.K., Nelson, R.A., Patton, T.L., Munn, S.G., 1990. Transfer zones in the east African rift system and their relevance to hydrocarbon exploration in rifts. American Association of Petroleum Geologists Bulletin 74, 1234–1253.
Nahm, A.L., Schultz, R.A., 2007. Outcrop-scale physical properties of Burns Formation at Meridiani Planum, Mars. Geophysical Research Letters 34, L20203. doi:10.1029/2007GL031005.
Nemčok, M., Schamel, S., Gayer, R., 2005. Thrustbelts: Structural Architecture, Thermal Regimes, and Petroleum Systems. Cambridge University Press.
Neuffer, D.P., Schultz, R.A., 2006. Mechanisms of slope failure in Valles Marineris, Mars. Quarterly Journal of Engineering Geology and Hydrogeology 39, 227–240.
Nimmo, F., 2004. Stresses generated in cooling viscoelastic ice shells: application to Europa. Journal of Geophysical Research 109, E12001. doi:10.1029/2004JE002347.
Nimmo, F., Giese, B., Pappalardo, R.T., 2003. Estimates of Europa's ice shell thickness from elastically-supported topography. Geophysical Research Letters 30, 1233. doi:10.1029/2002GL016660.

Nimmo, F., Schenk, P., 2006. Normal faulting on Europa: implications for ice shell properties. Journal of Structural Geology 28, 2194–2203.
Nimmo, F., Spencer, J.R., Pappalardo, R.T., Mullen, M.E., 2007. Shear heating as the origin of the plumes and heat flux on Enceladus. Nature 447, 289–291.
Ojakangas, G.W., Stevenson, D.J., 1989a. Thermal state of an ice shell on Europa. Icarus 81, 220–241.
Ojakangas, G.W., Stevenson, D.J., 1989b. Polar wander of an ice shell on Europa. Icarus 81, 242–270.
Okubo, C.H., Schultz, R.A., 2004. Mechanical stratigraphy in the western equatorial region of Mars based on thrust fault-related fold topography and implications for near-surface volatile reservoirs. Geological Society of America Bulletin 116, 594–605.
Okubo, C.H., Schultz, R.A., 2006a. Variability in Early Amazonian Tharsis stress state based on wrinkle ridges and strike-slip faulting. Journal of Structural Geology 28, 2169–2181.
Okubo, C.H., Schultz, R.A., Stefanelli, G.S., 2004. Gridding Mars Orbiter Laser Altimeter data with GMT: effects of pixel size and interpolation methods on DEM integrity. Computers and Geosciences 30, 59–72.
Okubo, C.H., Schultz, R.A., 2006b. Near-tip stress rotation and the development of deformation band stepover geometries in mode II. Geological Society of America Bulletin 118, 343–348. doi:10.1130/B25820.1.
Okubo, C.H., McEwen, A.S., 2007. Fracture controlled paleo-fluid flow in Candor Chasma, Mars: early results from MRO HiRISE. Science 315, 983–985. doi:10.1126/science.1136855.
Okubo, C.H., Lewis, K.L., McEwen, A.S., Kirk, R.L., 2008. Relative age of interior layered deposits in southwest Candor Chasma based on high-resolution structural mapping. Journal of Geophysical Research 113, E12002. doi:10.1029/2008JE003181.
Okubo, C.H., Schultz, R.A., Chan, M.A., Komatsu, G., HiRISE Team, 2009. Deformation band clusters on Mars and implications for subsurface fluid flow. Geological Society of America Bulletin 121, 474–482. doi:10.1130/B26421.1.
Okubo, C.H. Structural geology of Amazonian-aged layered sedimentary deposits in southwest Candor Chasma, Mars. Icarus, in press, doi:10.1016/j.icarus.2009.11.012.
Olson, J.E., 2003. Sublinear scaling of fracture aperture versus length: an exception or the rule? Journal of Geophysical Research 108, 2413. doi:10.1029/2001JB000419.
Pappalardo, R.T., Collins, G.C., 2005. Strained craters on Ganymede. Journal of Structural Geology 27, 827–838.
Pati, J.K., Reimold, W.U., 2007. Impact cratering: fundamental process in geoscience and planetary science. Journal of Earth System Science 116, 81–98.
Peacock, D.C.P., 2002. Propagation, interaction and linkage in normal fault systems. Earth-Science Reviews 58, 121–142.
Peacock, D.C.P., Sanderson, D., 1991. Displacements, segment linkage and relay ramps in normal fault zones. Journal of Structural Geology 13, 721–733.
Peulvast, J.P., Masson, P.L., 1993. Erosion and tectonics in central Valles Marineris (Mars): a new morpho-structural model. Earth Moon and Planets 61, 191–217. doi:10.1007/BF00572245.
Peulvast, J.-P., Mège, D., Chiciak, J., Costard, F., Masson, P., 2001. Morphology, evolution, and tectonics of Valles Marineris wallslopes (Mars). Geomorphology 37, 329–352. doi:10.1016/S0169-555X(00)00085-4.
Phillips, R.J., Conel, J.E., Abbott, E.A., Sjogren, W.L., Morton, J.B., 1972. Mascons: progress toward a unique solution for mass distribution. Journal of Geophysical Research 77, 7106–7114.
Phillips, R.J., Zuber, M.T., Solomon, S.C., Golombek, M.P., Jakosky, B.M., Banerdt, W.B., Smith, D.E., Williams, R.M.E., Hynek, B.M., Aharonson, O., Hauck II, S.A., 2001. Ancient geodynamics and global-scale hydrology on Mars. Science 291, 2587–2591.
Plescia, J.B., Golombek, M.P., 1986. Origin of planetary wrinkle ridges based on the study of terrestrial analogs. Geological Society of America Bulletin 97, 1289–1299.
Polit, A.T., Schultz, R.A., Soliva, R., 2009. Geometry, displacement-length scaling, and extensional strain of normal faults on Mars with inferences on mechanical stratigraphy of the Martian crust. Journal of Structural Geology 31, 662–673.
Pollard, D.D., 1987. Elementary fracture mechanics applied to the structured interpretation of dykes. In: Halls, H.C., Fahrig, W.F. (Eds.), Mafic Dyke Swarms. Geological Association of Canada Special Paper 34, 5–24.
Pollard, D.D., Segall, P., 1987. Theoretical displacements and stresses near fractures in rock: with applications to faults, joints, veins, dikes, and solution surfaces. In: Atkinson, B.K. (Ed.), Fracture Mechanics of Rock. Academic Press, London, pp. 277–349.
Porco, C.C., Helfenstein, P., Thomas, P.C., Ingersoll, A.P., Wisdom, J., West, R., Neukum, G., Denk, T., Wagner, R., Roatsch, T., Kieffer, S., Turtle, E., McEwen, A., Johnson, T.V., Rathbun, J., Veverka, J., Wilson, D., Perry, J., Spitale, J., Brahic, A., Burns, J.A., DelGenio, A.D., Dones, L., Murray, C.D., Squyres, S., 2006. Cassini observes the active south pole of Enceladus. Science 311, 1393–1401.
Price, N.J., Cosgrove, J.W., 1990. Analysis of Geological Structures. Cambridge University Press.
Prockter, L.M., Nimmo, F., Pappalardo, R.T., 2005. A shear heating origin for ridges on Triton. Geophysical Research Letters 32, L14202. doi:10.1029/2005GL022832.
Prockter, L.M., Head, J., Pappalardo, R., Sullivan, R., Clifton, A.E., Giese, B., Wagner, R., Neukum, G., 2002. Morphology of Europan bands at high resolution: a mid-ocean ridge-type rift mechanism. Journal of Geophysical Research 107, 1–26.
Prockter, L.M., Pappalardo, R.T., 2000. Folds on Europa: implications for crustal cycling and accommodation of extension. Science 289, 941–943.
Prockter, L.M., Ernst, C.M., Denevi, B.W., Chapman, C.R., Solomon, S.C., Blewett, D.T., Head, J.W., Cremonese, G., Marchi, S., Massironi, M., Marline, W.J. Evidence for young volcanism on Mercury from MESSENGER's third flyby. Proc. Lunar Sci. Conf. XXXXI, abstract, in press.
Radebaugh, J., Kirk, R.L., Lopes, R.M., Stofan, E.R., Valora, P., Lunine, J.I., Lorenz, R.D., the Cassini Radar Team, 2008. Mountains on Titan as evidence of global tectonism and erosion. Lunar and Planetary Science Conference XXXIX, abstract 2206.
Radebaugh, J., Valora, P., Lorenz, R.D., Wall, S.D., Kirk, R.L., Wood, C.A., Lunine, J.I., Stofan, E.R., Lopes, R.M., Farr, T.G., Mitri, G., Cassini Radar Team, 2009. Evidence of extensional and compressional tectonism and erosion in Titan's Xanadu Province. Lunar and Planetary Science Conference XL, abstract 1037.
Ramsay, J.G., Huber, M.I., 1987. The Techniques of Modern Structural Geology. In: Folds and Fractures, vol. 2. Academic Press, London, 462 pp.
Roatsch, Th., Wälisch, M., Giese, B., Hoffmeister, A., Matz, K.-D., Scholten, F., Kuhn, F., Wagner, R., Neukum, G., Helfenstein, P., Porco, C., 2008. High-resolution Enceladus atlas derived from Cassini-ISS images. Planetary and Space Science 56, 109–116.
Roering, J.J., Cooke, M.L., Pollard, D.D., 1997. Why blind thrust faults do not propagate to the Earth's surface: numerical modeling of coseismic deformation associated with thrust-related anticlines. Journal of Geophysical Research 102, 11901–11912. doi:10.1029/97JB00680.
Rudolph, M.L., Manga, M., 2008. Fracture penetration in planetary ice shells. Icarus 199, 536–541.
Schenk, P., Bulmer, M., 1998. Origin of mountains on Io by thrust faulting and large-scale mass movements. Science 279, 1514–1518.
Schenk, P., McKinnon, W.B., 1989. Fault offsets and lateral crustal movement on Europa: evidence for a mobile ice shell. Icarus 79, 75–100.
Schlische, R.W., Young, S.S., Ackerman, R.V., Gupta, A., 1996. Geometry and scaling relations of a population of very small rift related normal faults. Geology 24, 683–686.
Scholten, F., Gwinner, K., Roatsch, T., Matz, K.-D., Wählisch, M., Giese, B., Oberst, J., Jaumann, R., Neukum, G., the HRSC Co-Investigator Team, 2005. Mars Express HRSC data processing: methods and operational aspects. Photogrammetric Engineering and Remote Sensing 71, 1143–1152.
Schultz, P.H., 1976. Moon Morphology. U. Texas Press, Austin, 641 pp.
Schultz, R.A., 1989. Strike-slip faulting of ridged plains near Valles Marineris, Mars. Nature 341, 424–426.
Schultz, R.A., 1996. Relative scale and the strength and deformability of rock masses. Journal of Structural Geology 18, 1139–1149. doi:10.1016/0191-8141(96)00045-4.
Schultz, R.A., 1997. Displacement-length scaling for terrestrial and Martian faults: implications for Valles Marineris and shallow planetary grabens. Journal of Geophysical Research 102, 12009–12015. doi:10.1029/97JB00751.
Schultz, R.A., 1998. Multiple-process origin of Valles Marineris basins and troughs, Mars. Planetary and Space Science 46, 827–829. doi:10.1016/S0032-0633(98)00030-0.
Schultz, R.A., 1999. Understanding the process of faulting: selected challenges and opportunities at the edge of the 21st century. Journal of Structural Geology 21, 985–993.
Schultz, R.A., 2000a. Localization of bedding plane slip and backthrust faults above blind thrust faults: keys to wrinkle ridge structure. Journal of Geophysical Research 105, 12035–12052.
Schultz, R.A., 2000b. Fault-population statistics at the Valles Marineris extensional province, Mars: implications for segment linkage, crustal strains, and its geodynamical development. Tectonophysics 316, 169–193.
Schultz, R.A., 2002. Stability of rock slopes in Valles Marineris, Mars. Geophysical Research Letters 29, 1932. doi:10.1029/2002GL015728.
Schultz, R.A., 2009. Scaling and paleodepth of compaction bands, Nevada and Utah. Journal of Geophysical Research 114, B03407. doi:10.1029/2008JB005876.
Schultz, R.A., Fossen, H., 2002. Displacement-length scaling in three dimensions: the importance of aspect ratio and application to deformation bands. Journal of Structural Geology 24, 1389–1411. doi:10.1016/S0191-8141(01)00146-8.
Schultz, R.A., Fossen, H., 2008. Terminology for structural discontinuities. American Association of Petroleum Geologists Bulletin 92, 853–867.
Schultz, R.A., Mège, D., Diot, H., 2008a. Emplacement conditions of igneous dikes in Ethiopian traps. Journal of Volcanology and Geothermal Research 178, 673–692.
Schultz, R.A., Soliva, R., Fossen, H., Okubo, C.H., Reeves, D.M., 2008b. Dependence of displacement-length scaling relations for fractures and deformation bands on the volumetric changes across them. Journal of Structural Geology 30, 1405–1411.
Schultz, R.A., Moore, J.M., Grosfils, E.B., Tanaka, K.L., Mège, D., 2007. The Canyonlands model for planetary grabens: revised physical basis and implications. In: Chapman, M.G. (Ed.), The Geology of Mars: Evidence from Earth-Based Analogues. Cambridge University Press, pp. 371–399.
Schultz, R.A., Okubo, C.H., Goudy, C.L., Wilkins, S.J., 2004. Igneous dikes on Mars revealed by MOLA topography. Geology 32, 889–892.
Schultz, R.A., Okubo, C.H., Wilkins, S.J., 2006. Displacement-length scaling relations for faults on the terrestrial planets. Journal of Structural Geology 28, 2182–2193.
Schultz, R.A., Soliva, R., Okubo, C.H., Mège, D., 2010. Fault populations. In: Watters, T.R., Schultz, R.A. (Eds.), Planetary Tectonics. Cambridge University Press, pp. 457–510.
Smith, D.E., Zuber, M.T., Frey, H.V., Garvin, J.B., Head, J.W., Muhleman, D.O., Pettengill, G.H., Phillips, R.J., Solomon, S.C., Zwally, H.J., Banerdt, W.B., Duxbury, T.C., Golombek, M.P., Lemoine, F.G., Neumann, G.A., Rowlands, D.D., Aharonson, O., Ford, P.G., Ivanov, A.B., Johnson, C.L., McGovern, P.J., Abshire, J.B.,

Afzal, R.S., Sun, X., 2001. Mars Orbiter Laser Altimeter: experiment summary after the first year of global mapping of Mars. Journal of Geophysical Research 106, 23689–23722. doi:10.1029/2000JE001364.
Smith-Konter, B., Pappalardo, R.T., 2008. Tidally driven stress accumulation and shear failure of Enceladus's tiger stripes. Icarus 198, 435–451.
Soliva, R., Schultz, R.A., 2008. Distributed and localized faulting in extensional settings: insight from the North Ethiopian Rift – Afar transition area. Tectonics 27, TC2003. doi:10.1029/2007TC002148.
Soliva, R., Schultz, R.A., Benedicto, A., 2005. Three-dimensional displacement-length scaling and maximum dimension of normal faults in layered rocks. Geophysical Research Letters 32, L16302. doi:10.1029/2005GL023007.
Solomon, S.C., Head, J.W., 1979. Vertical movements in mare basins: relation to mare emplacement, basin tectonics, and lunar thermal history. Journal of Geophysical Research 84, 1667–1682.
Solomon, S.C., Head, J.W., 1980. Lunar mascon basins: lava filling, tectonics, and evolution of the lithosphere. Reviews of Geophysics 18, 107–141.
Solomon, S.C., McNutt Jr., R.L., Gold, R.E., Domingue, D.L., 2007. MESSENGER mission overview. Space Science Reviews 131, 3–39.
Solomon, S.C., McNutt, R.L., Watters, T.R., Lawrence, D.J., Feldman, W.C., Head, J.W., Krimigis, S.M., Murchie, S.L., Phillips, R.J., Slavin, J.A., Zuber, M.T., 2008. Return to Mercury: a global perspective on MESSENGER's first Mercury flyby. Science 321, 59–62.
Squyres, S.W., et al., 2006. Two years at Meridiani Planum: results from the Opportunity rover. Science 313, 1403–1407.
Strom, R.G., 1972. Lunar mare ridges, rings and volcanic ring complexes. Modern Geology 2, 133–157.
Strom, R.G., Trask, N.J., Guest, J.E., 1975. Tectonism and volcanism on Mercury. Journal of Geophysical Research 80, 2478–2507.
Tanaka, K.L., Golombek, M.P., Banerdt, W.B., 1991. Reconciliation of stress and structural histories of the Tharsis region of Mars. Journal of Geophysical Research 96, 15617–15633.
Tanaka, K.L., Anderson, R., Dohm, J.M., Hansen, V., McGill, G., Pappalardo, R., Schultz, R.A., Watters, T.R., 2010. Planetary structural mapping. In: Watters, T.R., Schultz, R.A. (Eds.), Planetary Tectonics. Cambridge University Press, pp. 351–396.
Tembe, S., Baud, P., Wong, T.-f., 2008. Stress conditions for the propagation of discrete compaction bands in porous sandstone. Journal of Geophysical Research 113, B09409. doi:10.1029/2005JB003611.
Trudgill, B., Cartwright, J., 1994. Relay-ramp forms and normal-fault linkages, Canyonlands National Park, Utah. Geological Society of America Bulletin 106, 1143–1157.
Turcotte, D.L., Schubert, G., 2002. Geodynamics, second ed. Cambridge University Press, New York, 456 pp.
Wahr, J., Selvans, Z.A., Mullen, M.E., Barr, A.C., Collins, G.C., Selvans, M.M., Pappalardo, R.T., 2009. Modeling stresses on satellites due to nonsynchronous rotation and orbital eccentricity using gravitational potential theory. Icarus 200, 188–206.
Watters, T.R., 1988. Wrinkle ridge assemblages on the terrestrial planets. Journal of Geophysical Research 93, 10236–10254.
Watters, T.R., Johnson, C., 2010. Lunar Tectonics. In: Watters, T.R., Schultz, R.A. (Eds.), Planetary Tectonics. Cambridge University Press, pp. 121–182.
Watters, T.R., Nimmo, F., 2010. The tectonics of Mercury. In: Watters, T.R., Schultz, R.A. (Eds.), Planetary Tectonics. Cambridge University Press, pp. 15–80.
Watters, T.R., Robinson, M.S., Cook, A.C., 1998. Topography of lobate scarps on Mercury: new constraints on the planet's contraction. Geology 26, 991–994.
Watters, T.R., Schultz, R.A., Robinson, M.S., 2000. Displacement-length scaling relations of thrust faults associated with lobate scarps on Mercury and Mars: comparison with terrestrial faults. Geophysical Research Letters 27, 3659–3662.
Watters, T.R., Schultz, R.A., Robinson, M.S., Cook, A.C., 2002. The mechanical and thermal structure of Mercury's early lithosphere. Geophysical Research Letters 29, 371–374. doi:10.1029/2001GL014308.
Watters, T.R., Schultz, R.A. (Eds.), 2010. Planetary Tectonics. Cambridge University Press, p. 518.
Watters, T.R., Solomon, S.C., Robinson, M.S., Head, J.W., André, S.L., HauckII, S.A., Murchie, S.L., 2010. The tectonics of Mercury: the view after MESSENGER's first flyby. Earth and Planetary Science Letters 285, 283–296. doi:10.1016/j.epsl.2009.01.025.
Watters, T.R., Murchie, S.L., Robinson, M.S., Solomon, S.C., Denevi, B.W., André, S.L., Head, J.W., 2009a. Emplacement and tectonic deformation of smooth plains in the Caloris basin. Mercury. Earth and Planetary Science Letters 285, 309–319. doi:10.1016/j.epsl.2009.03.040.
Watters, T.R., Head, J.W., Solomon, S.C., Robinson, M.S., Chapman, C.R., Denevi, B.W., Fassett, C.I., Murchie, S.L., Strom, R.G., 2009b. Evolution of the Rembrandt impact basin on Mercury. Science 324, 618–621.
Watts, A.B., 2001. Isostasy and Flexure of the Lithosphere. Cambridge University Press, Cambridge, U.K., 478 pp.
Wilhelms, D.E., 1987. The geologic history of the Moon. U.S. Geological Survey Professional Paper 1348.
Wilkins, S.J., Schultz, R.A., Anderson, R.C., Dohm, J.M., Dawers, N.C., 2002. Deformation rates from faulting at the Tempe Terra extensional province, Mars. Geophysical Research Letters 29, 1884. doi:10.1029/2002GL015391.
Wise, D.U., Golombek, M.P., McGill, G.E., 1979. Tharsis province of Mars: geologic sequence, geometry, and a deformation mechanism. Icarus 38, 456–472.